Three-dimensional numerical simulations of crustal systems undergoing orogeny and subjected to surface processes

C Thieulot, P Steer, Ritske Huismans

RESEARCH ARTICLE

Three-dimensional numerical simulations of crustal systems undergoing orogeny and subjected to surface processes

C. Thieulot[1,2,3], P. Steer[1,4], and R. S. Huismans[1]

[1]Department of Earth Science, Bergen University, Bergen, Norway, [2]Now at CEED, University of Oslo, Norway, [3]Also at Department of Earth Sciences, Utrecht University, The Netherlands, [4]Now at Géosciences Rennes, UMR 6118, Université de Rennes, Rennes Cedex, France

Abstract As several modeling studies indicate, the structural expression and dynamic behavior of orogenic mountain belts are dictated not only by their rheological properties or by far-field tectonic motion, but also by the efficiency of erosion and sedimentation acting on its surface. Until recently, numerical investigations have been mainly limited to 2-D studies because of the high computational cost required by 3-D models. Here, we have efficiently coupled the landscape evolution model Cascade with the 3-D thermomechanically coupled tectonics code FANTOM. Details of the coupling algorithms between both codes are given. We present results of numerical experiments designed to study the response of viscous-plastic crustal materials subjected to convergence and to surface processes including both erosion and sedimentation. In particular, we focus on the equilibration of both the tectonic structures and on the surface morphology of the orogen. We show that increasing the efficiency of fluvial erosion increases the frontal thrust angle, which in turn decreases the width of the orogen. In addition, the maximum summit elevation of the orogen during transient evolution is significantly higher in those models showcasing surface processes than those that do not. This illustrates the strong coupling between tectonics and surface processes. We also demonstrate that an along-strike gradient of erosion efficiency can have a major impact upon the landscape morphology and the tectonic structure and deformation of the orogen, in both the across-strike and along-strike directions. Overall, our results suggest that surface processes, by enhancing localization of deformation, can act as a positive forcing to topographic building.

1. Introduction

It is accepted that the topographic evolution of orogenic mountain belts results from interactions between tectonics and surface processes [e.g., *Koons*, 1990; *Molnar and England*, 1990; *Beaumont et al.*, 1992; *Avouac and Burov*, 1996; *Willett*, 1999; *Whipple*, 2009; *Vernant et al.*, 2013]. For instance, supply-limited rivers in a mountain range may lead to rapid erosion and thus to a rapid rock uplift in the area [*Koons*, 1998; *Zeitler et al.*, 2001; *Koons et al.*, 2002]. At a larger scale, surface processes modify the balance between gravitational stresses, owing to the topographic load of the mountain belt, and the tectonic forces resulting from relative plate motions. This imbalance can lead to perturbation of plate tectonic relative motion [*Iaffaldano et al.*, 2006, 2011] or orogen internal dynamics [*Braun*, 2010; *Steer et al.*, 2014]. This latter case is supported by analytical, analog, and numerical models, all of which demonstrate that orogen internal structure is influenced by both its rheological properties and surface processes [e.g., *Dahlen et al.*, 1984; *Koons*, 1990, 1994; *Dahlen*, 1990; *Beaumont et al.*, 1992; *Willett et al.*, 1993; *Willett*, 1999; *Montgomery and Brandon*, 2002; *Hilley and Strecker*, 2004; *Whipple and Meade*, 2004, 2006; *Persson et al.*, 2004; *Roe et al.*, 2008; *Braun and Yamato*, 2010; *Graveleau et al.*, 2011; *Roe and Brandon*, 2011; *Erdös et al.*, 2014; *Steer et al.*, 2014].

Among these approaches, numerical models offer quantitative insight into the interactions between tectonics and surface processes. Coupling between tectonic processes and surface processes has mostly been accounted for by 2-D cross-section view tectonic models coupled with 1-D [*Kooi and Beaumont*, 1994; *Avouac and Burov*, 1996; *Beaumont et al.*, 1996; *Garcia-Castellanos et al.*, 1997; *Burov and Cloetingh*, 1997; *Batt and Braun*, 1997, 1999; *Willett*, 1999; *Burov and Poliakov*, 2001; *Toussaint et al.*, 2004; *Pysklywec*, 2006; *Simpson*, 2006; *Burov and Toussaint*, 2007; *Kaus et al.*, 2008; *Selzer et al.*, 2008] or 2-D surface process models [*Beaumont et al.*, 1992; *Godard et al.*, 2004; *Lavé*, 2005; *Stolar et al.*, 2006; *Godard et al.*, 2006; *Stolar et al.*, 2007; *Willett*, 2010] and 2-D (or 3-D thin sheet) plan-view tectonic model coupled with 2-D surface process

model [*Masek et al.*, 1994; *Braun and Shaw*, 2001; *Garcia-Castellanos*, 2002; *Fischer et al.*, 2004; *Simpson*, 2004; *Stüwe et al.*, 2008]. Because of the high computational cost associated with 3-D models, only a few studies have investigated the interactions between tectonics and surface processes in a fully coupled 3-D dynamic approach [*Koons et al.*, 2002; *Kurfess and Heidbach*, 2009; *Maniatis et al.*, 2009; *Braun and Yamato*, 2010; *Colligon et al.*, 2014]. However, 3-D models are required to understand better the dynamics of mountain belts that exhibit strong 3-D deformation pattern, such as the Southern Alps of New-Zealand [*Tomkin and Braun*, 1999; *Gerbault et al.*, 2003; *Upton and Koons*, 2007; *Upton et al.*, 2009; *Castelltort et al.*, 2012].

Here we present results from a new 3-D numerical model that couples the thermomechanical code FAN-TOM [*Thieulot*, 2011] with the surface process code Cascade [*Braun and Sambridge*, 1997]. In particular, we design numerical experiments to study the response of viscous-plastic crustal materials subjected to both convergence and surface processes. The intention of our study is twofold. First, we explain the modeling approach and describe in detail the principle of the coupling between surface processes and tectonic deformation. Second, we use this new 3-D model to investigate the structural and dynamic expression of a thermomechanically coupled crustal orogen subjected to surface processes of varying intensity.

2. Governing Equations

2.1. Tectonics

The tectonics equations are solved numerically by means of the 3-D parallel finite element code FANTOM [*Thieulot*, 2011]. It is assumed that (1) on geological time scales, the Earth's lithosphere deforms at a sufficiently low rate that inertial forces can be neglected; and (2) that rocks behave like an incompressible visco-plastic fluid that obeys the following equations:

$$\nabla \cdot \boldsymbol{\sigma} + \rho \boldsymbol{g} = \boldsymbol{0} \tag{1}$$

$$\nabla \cdot \boldsymbol{v} = 0 \tag{2}$$

with

$$\boldsymbol{\sigma} = -p\mathbf{1} + \boldsymbol{s} \tag{3}$$

$$p = -\frac{1}{3} Tr[\boldsymbol{\sigma}] \tag{4}$$

$$\boldsymbol{s} = 2\mu\dot{\boldsymbol{\epsilon}} \tag{5}$$

$$\dot{\boldsymbol{\epsilon}} = \frac{1}{2}\left(\nabla\boldsymbol{v} + (\nabla\boldsymbol{v})^T\right) \tag{6}$$

where $\boldsymbol{\sigma}$ is the stress tensor, $\mathbf{1}$ is the unit tensor, ρ is the density, $\boldsymbol{g}$ is the acceleration owing to gravity, p is the pressure, μ is the dynamic viscosity, $\dot{\boldsymbol{\epsilon}}$ is the strain-rate tensor, $\boldsymbol{v}$ is the velocity vector, and $\boldsymbol{s}$ is the deviatoric stress tensor. Supplied with appropriate boundary conditions (see section 4), equations (1), (2), (3), (5), and (6) form a closed set of equations that allow us to compute the velocity and pressure (our primary variables).

Rock material properties such as density and viscosity depend on temperature. It is therefore necessary to compute the temperature field within the deforming system by solving the heat transport equation:

$$\rho c_p \left(\frac{\partial T}{\partial t} + \boldsymbol{v} \cdot \nabla T\right) = \nabla \cdot (k\nabla T) + \rho H \tag{7}$$

where T is the absolute temperature, k is the thermal conductivity, c_p is the heat capacity, and H is the radiogenic heat production per unit mass (shear-heating and adiabatic-heating effects are neglected). Also, the mass density ρ varies as a function of temperature according to:

$$\rho(T) = \rho_0(1 - \alpha(T - T_0)) \tag{8}$$

where α is the thermal expansion coefficient and ρ_0 is the reference density at the reference temperature T_0.

2.2. Rheology and Material Memory

In what follows, we only consider the long-term deformation of a crustal layer, approximated by a single viscoplastic material. The rheological behavior at a given location in space is dynamically determined by both

pressure and temperature fields at this location. Close to the surface, temperatures, and pressures are low, leading to a brittle behavior characteristic of the uppercrust, while at depth temperatures and pressures increase, leading to nonlinear temperature-dependent viscous deformation being the dominant deformation mechanism.

In the context of continuum mechanics, brittle failure is approximated by a viscous deformation following a plasticity criterion. Viscosity values are locally adapted to limit the stress that is generated during deformation. The plasticity model used is the pressure-dependent Mohr-Coulomb model [*Braun et al.*, 2008]. The yield criterion is calculated using

$$F = (J_2')^{\frac{1}{2}} - \sigma_Y(c, p, \phi) \tag{9}$$

where J_2' is the second invariant of the deviatoric stress tensor (see Appendix B of *Thieulot* [2011]), σ_Y is the yield value, c is the cohesion, and ϕ is the angle of internal friction. If $F > 0$ the brittle behavior dominates, while if $F < 0$ the deformation follows the viscous branch. Initially, the yield value is fixed at

$$\sigma_Y = p \sin \phi + c \cos \phi \tag{10}$$

but as tectonics proceed, strain gradually accumulates. When it reaches a user-defined threshold value ε_1, the material starts to strain-weaken, and σ_Y decreases with strain until strain reaches a second threshold value ε_2, above which the yield value reaches its final strain weakened value σ_Y^{sw} [*Allken et al.*, 2011] given by

$$\sigma_Y^{sw} = p \sin \phi^{sw} + c^{sw} \cos \phi^{sw} \tag{11}$$

where c^{sw} and ϕ^{sw} are the strain-weakened cohesion and angle of friction, respectively.

Nonlinear viscous deformation in the lower crust is approximated by a strain rate-dependent and thermally activated viscosity. This power-law rheology is described by the nonlinear equation:

$$\mu_{eff} = \frac{1}{2} B^{-1/n} (E_2')^{1/n-1} \exp \left(\frac{Q}{nRT} \right) \tag{12}$$

where E_2' is the second invariant of the strain rate tensor, A is a material constant, n is the stress exponent, Q is the creep activation energy, R is the gas constant. A, n, and Q are empirically determined material-dependent constants that it is assumed will not vary with stress or (p, T) conditions.

3. Numerical Implementation

3.1. FANTOM
FANTOM [*Thieulot*, 2011] resorts to an Arbitrary Lagrangian-Eulerian (ALE) kinematic description of the rock flow field and solves for primary variables velocity **v** and pressure p. The key idea in the ALE formulation is the introduction of a computational grid that can move and deform with a velocity independent of the velocity carried by the Lagrangian material particles. At start-up, the computational domain is a cuboid of size $L_x \times L_y \times L_z$. A $nnx \times nny \times nnz$ rectangular grid spanning the simulation domain is created. The FANTOM-free surface (hereafter referred to as the *F*-surface) is therefore composed of $nnx \times nny$ grid nodes constituting the top layer of the grid, which are free to move vertically.

The velocity field is computed on the grid nodes but their movement is ultimately only allowed in the *z*-direction (see Figure 4 of *Thieulot* [2011]). Indeed the horizontal dimensions of the computational domain remain fixed at L_x and L_y, while the vertical position of the nodes composing the *F*-surface account for the change in topography.

Material tracking is carried out by means of the cloud of Lagrangian material particles of self-adapting number density. The particles are advected with a velocity obtained by interpolation of the computed velocity by means of the finite element linear shape functions. The advection time step δt_F is computed by means of a CFL criterion with a CFL number $C = 0.1$. Finite strain is computed and stored on these points and is used to include the effects of strain weakening.

The viscosity rescaling method is implemented in the plastic model during the finite element matrix building process [*Willett*, 1999; *Fullsack*, 1995; *Thieulot et al.*, 2008], resulting in an effective viscosity in the

frictional-plastic regions (low in shear zones, high in rigid blocks), and a physical viscosity in the viscous regions.

3.2. Cascade

Many numerical models have been developed over the past three decades [*Coulthard*, 2001; *Crave and Davy*, 2001; *Braun*, 2006; *Willgoose*, 2005; *Davy and Lague*, 2009; *Tucker and Hancock*, 2010; *Braun and Willett*, 2013].

In this work, the top-free surface of the 3-D tectonic model is subjected to the planform surface process model Cascade, which includes hillslope processes and fluvial erosion and deposition. We will here limit ourselves to the description of its key features, as a full description can be found in *Braun and Sambridge* [1997].

Because fluvial incision is believed to be the controlling factor of landscape denudation [*Burbank et al.*, 1996], the fluvial component of any surface process model is therefore its most critical aspect.

In Cascade, river channels have a sediment-carrying capacity (i.e., sediment volume that can be carried per unit time), q_c, which is proportional to local slope, S, and drainage area, A (i.e., a proxy for local discharge)

$$q_c = K_f S A \tag{13}$$

where K_f is a constant (in $m.yr^{-1}$) that varies mostly with climate and precipitation rate (with higher K_f values corresponding to a higher precipitation rate).

Following the so-called "under-capacity" model for fluvial erosion and transport that is used within Cascade, we assume that a river channel will erode or deposit depending mainly on the relative value of sediment load, q_s, compared to river sediment carrying capacity. Where sediment load is smaller than the river capacity, erosion takes place, at a rate set by:

$$\frac{\partial h}{\partial t} = \frac{q_c - q_s}{w_f l_f} \tag{14}$$

where l_f is a length scale characterizing the erodibility of bedrock [*Kooi and Beaumont*, 1994] (with higher l_f values corresponding to more resistant rocks) and w_f is the river channel width, which is here assumed to be proportional to $A^{0.5}$ [e.g., *Leopold and Maddock*, 1953]. Where sediment load exceeds capacity, deposition takes place at a rate set by

$$\frac{\partial h}{\partial t} = \frac{q_s - q_c}{\Omega} \tag{15}$$

where Ω is the surface area attached to each node and defined by the spatial discretization, defined below.

Hillslope processes (landslides, soil creep, rain splash, etc.) are implemented by a linear diffusion equation, where the temporal change in elevation of a point is proportional to the second derivative of topography [*Kooi and Beaumont*, 1994; *Braun and Sambridge*, 1997]:

$$\frac{\partial h}{\partial t} = K_d \nabla^2 h \tag{16}$$

where K_d is the diffusivity (in $m^2.yr^{-1}$) and is a measure of the efficiency of the hillslope transport processes, which depends mainly on climate and lithology.

We here refer to the set of Cascade nodes as the *C*-surface. One of the main feature of Cascade is that it uses an irregular mesh instead of a square grid. Each node of the surface is linked to its direct neighbors by a Delaunay triangulation, and the associated Voronoi cell defines its representative surface area Ω [*Braun and Sambridge*, 1997]. The irregular nature of the mesh (1) prevents water-flow directional bias that arises in regular grids, and (2) allows for a direct 3-D advection of the Cascade nodes following the tectonic velocity computed by FANTOM. However, since Cascade uses an explicit time integration scheme that is only conditionally stable, it requires the use of small time steps δt_C, in contrast, for example, to the newly developed model Fastscape [*Braun and Willett*, 2013; *Croissant and Braun*, 2014].

3.3. Coupling FANTOM With Cascade
3.3.1. Basic Concept

In order to couple Cascade and FANTOM, which are based respectively on an irregular and a regular grid, we have designed an algorithm that allows us to transfer the elevation information between the Cascade
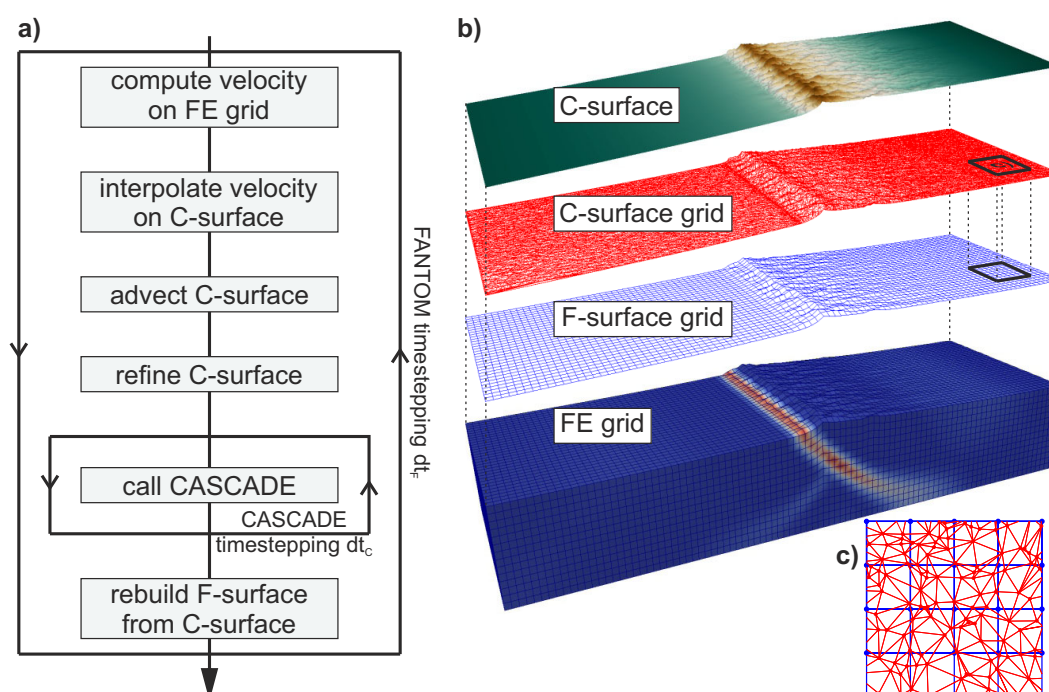
Figure 1. Illustration of the coupling between surface processes (Cascade) and tectonics (FANTOM). (a) Flowchart presenting the coupling algorithm; (b) illustration of the various objects and grids used by the numerical model: the *F*-surface is the top surface of the Finite Element (FE) grid, and the *C*-surface is the triangulated Cascade surface; (c) zoom on the regular *F*-surface (in blue) overlain by the randomly distributed and triangulated *C*-surface nodes (in red).

C-surface and the FANTOM *F*-surface (Figure 1). For every tectonic time step, the *C*-surface is subjected to the Cascade algorithm after it has been advected by tectonic transport. This implies an interpolation of velocities from the *F*-surface onto the *C*-surface. Conversely, the feedback of the surface process model on the tectonic model requires an interpolation of the *C*-surface elevation onto the *F*-surface. These interpolations are necessary due to the fact that the nodes of these two surfaces do not spatially coincide.

3.3.2. Interpolation and Time Stepping

On the one hand, the free surface of the FANTOM computational grid is composed of a regular arrangement of $nnx \times nny$ nodes spaced equidistantly in the xy-plane, whose elevation z is adjusted to track the location of the free surface. On the other hand, the surface process model Cascade operates best on a triangulated surface whose nodes are randomly distributed (Figure 1).

At the start, the elevation of the FE grid-free surface is $z = L_z$, and a triangulated surface is therefore created and placed at the same elevation. At every time step, the *C*-surface is first advected by tectonic transport: each surface process model node is projected onto the grid-free surface and the velocity field is interpolated at this location by means of the FE (linear) shape functions. While the interior nodes of the *C*-surface are advected in the *x*, *y*, *z* directions, those on its convex hull only move tangentially to the sides of the computational domain. Note that the *C*-surface is never regenerated, only advected and subjected to the Cascade model, so that drainage basins are conserved in between tectonic and erosional time steps.

The *C*-surface is then subjected to the surface process model Cascade. The surface process model generally requires smaller time steps than the tectonic model. Therefore, the FANTOM tectonic time step δt_F is broken down into many Cascade subtimesteps δt_C, thereby insuring the stability of the surface process model.

At the end of Cascade time stepping, information is transferred back to FANTOM by a moving least square interpolation of elevation from the *C*-surface to the *F*-surface.

3.3.3. Refining the C-Surface Node Density

Due to tectonic advection, the density of *C*-surface nodes evolves over time, which leads to areas showing rarefaction or accumulation of nodes. In order for the interpolation schemes (based on local methods) to remain accurate and to avoid unnecessary computations, a local addition and deletion of nodes and the
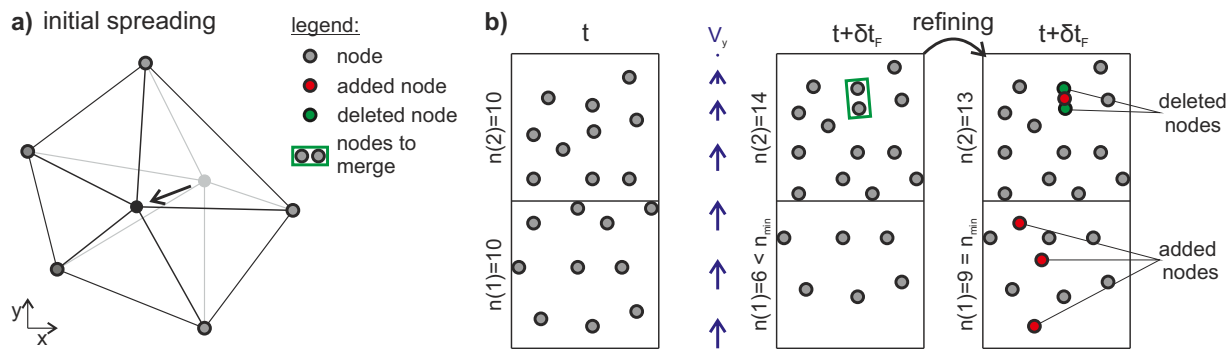
Figure 2. (a) Schematic representation of the initial C-surface node spreading by barycentering; (b) schematic C-surface refining by node addition and deletion. The model comprises two FANTOM square elements, each including $n(i) = 10$ C-surface nodes. The applied node velocity V_y between t and $t+\delta t_F$ results in moving some of the nodes from element 1 to 2, leading to both an addition of nodes in element 1 to respect the minimum node number n_{min}, and to merging of 2 nodes in element 2 because of a too short internodal distance.

consequent remeshing of the triangulated surface are therefore required (Figure 2). The deletion, addition, and triangulation of nodes are performed before the call to Cascade.

3.3.3.1. Spreading Points

While the Cascade C-surface is required to be an irregular mesh to avoid potential directional bias of water flow [*Braun and Sambridge*, 1997], too irregular a mesh is not appropriate from the perspective of the numerical methods employed in Cascade. An algorithm has therefore been designed to "smooth" the initially generated C-surface (Figure 2a), which proceeds as follows: (1) the direct neighbors of each node i of the C-surface that does not belong to the convex hull is computed; (2) the barycenter coordinates of these direct neighbors are computed and stored as the new coordinates of point i; and (3) once the new positions of all the nodes of the C-surface are known, their position is then updated.

3.3.3.2. Adding Points

The tectonic advection of the C-surface points in the x and y directions can rapidly lead to very scarce node distributions, especially in the foreland of mountain belts or in graben areas for contractional and extensional settings, respectively. We have implemented a dedicated algorithm (Figure 2b) that prevents the occurrence of low node density areas and enforces a high resolution for surface processes: (1) the number of C-surface nodes $n(ie)$ per square element ie of the F-surface in the xy-plane is computed; (2) if this number falls below a user-defined minimum number n_{min} (typically 3), then $n_{min} - n(ie)$ C-surface nodes are to be added in this element; and (3) the missing nodes are randomly added within the element and their elevation is computed with a local linear interpolation.

3.3.3.3. Removing Points

Conversely, the horizontal advection of the C-surface points can result in a very dense distribution of nodes, for example at mountain fronts or in horst areas. This progressive increase of node number density with time leads to a significant slowdown of the surface process model. In order to circumvent this problem, we have designed a node deletion/merging algorithm: (1) the distance d_{ij} between each pair i-j of direct neighbor nodes is computed; (2) if d_{ij} is less than a minimum user-defined distance d_{min} (typically $dx/20$ where dx is the grid spacing), then the nodes i and j are merged into a new node k, while i and j are deleted; and (3) the x, y, and z coordinates of the new node k are defined as the mean coordinates of the old nodes i and j (Figure 2b).

4. Model Setup

We have designed a series of numerical models to investigate the response of viscous-plastic crustal materials to both tectonics convergence and surface processes (Figure 3).

The model domain, including both a frictional-plastic uppercrust and a viscous lower-crust, has dimensions $L_x = 192 \mathrm{km} \times L_y = 64 \mathrm{km} \times L_z = 28 \mathrm{km}$. It is filled with wet quartz characterized by a viscoplastic rheology, whose rheological parameters are taken from *Tullis* [2002] and given in Table 1. Because we use only one set of
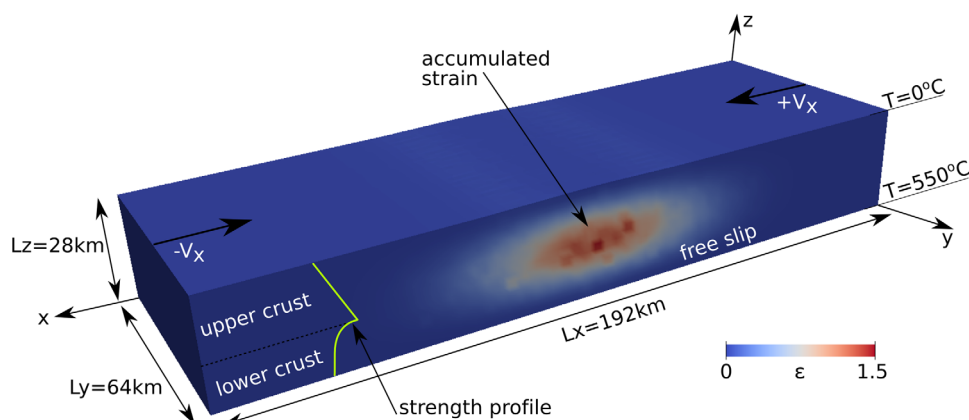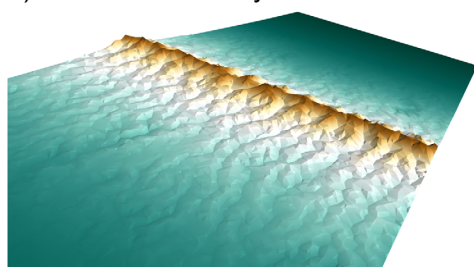
Figure 3. 3-D representation of the tectonic setup, showing the model dimensions, the velocity, and temperature boundary conditions, and the initial vertical strength profile. Lagrangian particles are given an initial strain value $s=a(1-\cos(2\pi x/L_x))^4(1-\cos(2\pi z/L_z))$ where a is a random value between 0 and 1, resulting in the shown initial accumulated strain ε distribution.
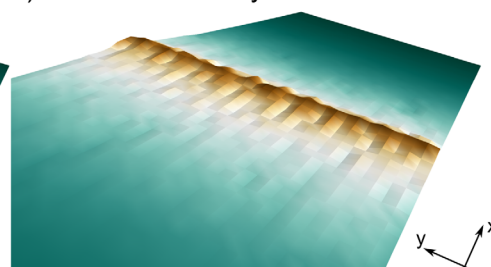
material properties for the entire crust, the depth-transition between the plastic uppercrust and the viscous lower-crust is therefore dynamically determined by the temperature and pressure distributions.

A temperature of $T=0°C$ is imposed on the free surface while $T=550°C$ is imposed at the bottom of the model ($z=0$). At startup, an initial linear temperature gradient is imposed between these two interfaces.

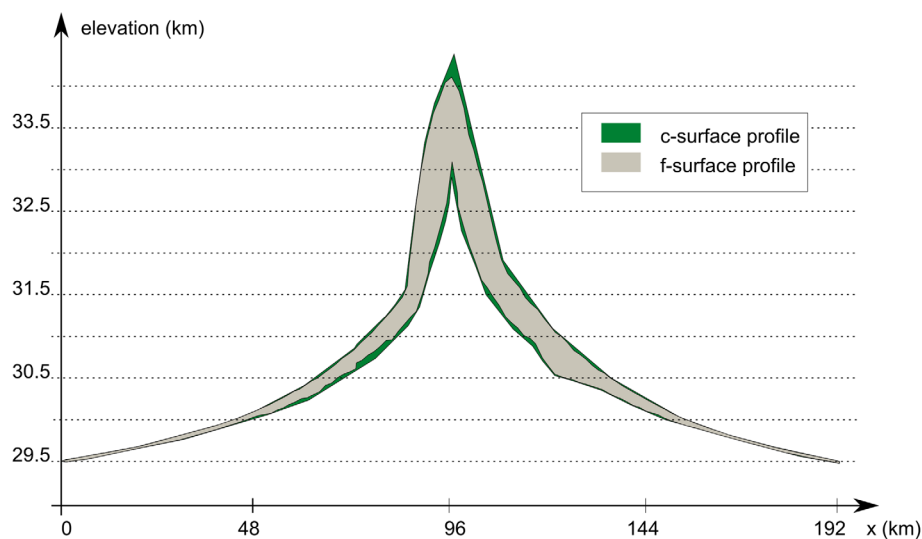**Figure 4.** (a) 3-D view of the Cascade C-surface of the reference model at $t=4$ Myrs; (b) corresponding FANTOM F-surface; (c) comparison of both swath profiles (surface topography projected along the y direction).

Table 1. Nomenclature and Reference Values for the Tectonic Parameters[a]

Symbol	Ref. Value	Meaning
δt_F	5000yr	FANTOM time step
L_x, L_y, L_z	192, 64, 28km	Domain dimensions
$\boldsymbol{g}$	$(0, 0, -9.81)\text{m.s}^{-2}$	Gravity acceleration
ρ_0	2800kg.m^{-3}	Mass density
V_x	$\pm 0.5\text{cm.yr}^{-1}$	Imposed convergence velocity
ϕ, ϕ^{sw}	$15^\circ, 2^\circ$	Angle of internal friction
c, c^{sw}	20MPa, 10MPa	Cohesion
ϵ_1, ϵ_2	0.25, 1.25	Strain thresholds
n	4	Power-law creep exponent
R	$8.3144\text{J.mol}^{-1}.\text{K}^{-1}$	Gas constant
Q	$223 \times 10^3 \text{J.mol}^{-1}$	Activation energy
B	$1.10 \times 10^{-28}\text{Pa}^{-n}.\text{s}^{-1}$	Power-law initial constant
α	$2.5 \times 10^{-5}\text{K}^{-1}$	Thermal expansion coefficient
c_P	$803.57\text{J.kg}^{-1}.\text{K}^{-1}$	Heat capacity
H	$0.9 \times 10^{-6}\text{W.m}^{-3}$	Heat production
k	$2.25\text{W.m}^{-1}.\text{K}^{-1}$	Heat conductivity

[a]Power-law rheology parameters from *Tullis* [2002], plastic rheology parameters from *Huismans and Beaumont* [2007], and other parameters from *Ranalli* [1995].

Convergent velocity boundary conditions are applied in the x direction with $V_x(x=0) = +0.5$ cm.yr^{-1} and $V_x(x=L_x) = -0.5$cm.yr^{-1}. No inward or outward flux of material is allowed through the lateral sides ($y=0, L_y$) and at the bottom of the box ($z = 0$) free-slip boundary conditions are used.

In contrast to *Willett* [1999] or *Braun and Yamato* [2010], we do not impose any basal velocity discontinuity in order to simulate a subduction-like process. Instead, we use an alternative approach, that was successfully applied to the modeling of divergent tectonic settings [*Allken et al.*, 2011, 2012], which consists in introducing initial rheological disconti-nuities to localize deformation. Here, a tubular-shape weak seed, orientated in the y direction, is introduced at the center of the model and at the base of the upper-crust to induce a weak-ness zone with respect to the main direction of convergence. Practically, cloud points are given an initial random strain value between 0 and 1.75 tapered in the x and z directions (Figure 3).

The computational grid has $96 \times 32 \times 14 = 43,008$ elements. This leads to a symmetric Stokes matrix of size $N = 144,045$, and a temperature matrix of size $N_T = 48,015$. Both matrices are solved by means of the WSMP direct solver Gupta [2000a, 2000b]. An average of 50 cloud points is placed per element so that there are approximately 2.2×10^6 Lagrangian markers present in the whole system. All the models presented in this work were run on a Cray XT4 supercomputer with 16 cores. On average a Stokes solve took 8.2 s, a temperature solve less than 1 s, and a call to Cascade between 25 and 35 s. Each run took approximately less than a day to run.

Cascade boundary conditions are such that sediments can only leave the domain through the edges paral-lel to the orogen (for $x = 0$ and $x = L_x$). There are at the beginning 4 Cascade points per element of the F-surface and this number is only allowed to increase over time with a limit set to 50 (see subsection 3.3.3). At startup, the points of C-surface have an elevation set to L_z with an additional random topography of ± 1m. Note that as the mechanical model thickens, the surface model base level is dynamically adapted. The ero-sion time step δ_C is fixed to 10 year so that 500 calls to Cascade are performed per tectonic time step (see Appendix A for a discussion on δt_F and δt_C).

For convenience, the notation, reference value, and unit of used quantities are summarized in Table 1.

5. Results

Before investigating the effect of varying erosion efficiency in the simulations coupling tectonic deforma-tion and surface processes, we first use the following model (coined hereafter "reference model") to illus-trate some of the main features of the coupling.

5.1. Reference Model

We choose for the reference model the following Cascade model parameters $K_f = 0.1$m.yr^{-1}, $l_f = 10$ km, and $K_d = 0.1$m^2.yr^{-1} which yield a realistic topography evolution. We let the simulation run for 6 Myr and then compare the C- and F-surface in both 3-D and in a profile (Figure 4). The C-surface displays the expected char-acteristics of an orogenic landscape incised by fluvial valleys. Note that Cascade does not allow for very fine dynamical modeling of the rivers morphology so that the description of the network topology is outside of the scope of this work (see *Whipple* [2004] for a review of bedrock rivers in the context of active orogens).

The F-surface, while at a coarser spatial resolution, presents similar features, albeit smoother. When both profiles are superimposed on a single plot (Figure 4c), one can verify that the different spatial resolutions of the surfaces and the constant interpolation between the two leads to very similar profiles. Owing to the

smoothing effect of the interpolation scheme, both the local topographic relief (i.e., valley to divide elevation) and the summit elevation of the *F*-surface are marginally smaller than for the *C*-surface.

One can now look at the time evolution of the *C*-surface. The influx of material through the boundaries of the model leads to both a global thickening of the crust and to an increase of the orogen elevation, as shown in Figure 5. Over the course of 6 Myr, the summit elevation evolves from 0 to about 5 km and the overall width of the orogen increases significantly. The development of topographic relief, at the scale of the orogen, is mainly the consequence of the localization of deformation that occurs on the shear zone(s) located on the side(s) of the orogen, while at smaller spatial-scales fluvial incision promotes relief development. However, we attribute the progressive thickening, of about 3–4 km of the entire model over 6 Myr to distributed deformation that occurs due to the no vertical-flux condition imposed at the base of the model. This boundary condition prevents the development of a crustal root or the initiation of subduction that we expect to preclude the general thickening of the model.

Figure 6 shows the time evolution of the coupling between tectonics and surface processes for this reference model up to $t = 4$ Myrs (the later stages are of importance in the context of the figure). After 500 kyr, the deformation is localized in two broad shear zones. A long-wavelength topography overlays the diffuse weak seed. At $t=1$ Myr, the strain-weakening feedback leads to localized shear zones, forming an angle of approximately 30° with the surface. At $t=2$ Myr, the shear zones are fully strain-weakened, resulting in localized asymmetric deformation. The angle of the shear zone has increased to 45°. After 3 Myr of tectonic deformation, the shear zones angle steepens even more, and the intersection of the shear zones has moved toward the free surface. At $t=4$ Myr, one of the shear zones has been abandoned in favor of the other, and the system is asymmetric [*Huismans et al.*, 2005]. This is also reflected in the topography with a narrow and steep mountain front on its active side (i.e., left) and a lower gradient on the abandoned shear zone side (i.e., right), which shows a network of low-gradient river and elongated valleys.

Looking at the timings of the various parts of the code for a typical simulation, we observe that the cost associated with the algorithms presented in subsection 3.3 (interpolation, refinement, addition, and removal of points performed on a *C*-surface containing about 14,000 points in total) is negligible ($<$1 s) compared to the average time spent in Cascade per time step ($\sim$25 s).

5.2. Parametric Investigation and Characteristic Features

We now turn to a parametric study of the influence of erosion efficiency on orogeny dynamics and structural style. Several parameters of the Cascade surface process model can be varied to control the efficiency of erosion: the hillslope diffusivity K_d, the fluvial erosion efficiency K_f, and transport length scale l_f. Even if
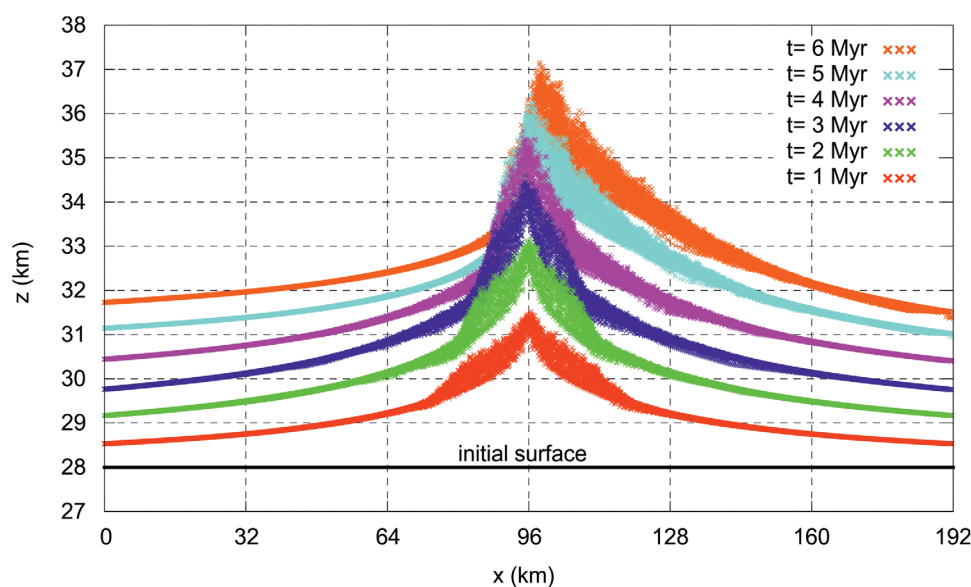
Figure 5. Topographic profiles (*C*-surface) as a function of time for the reference model. While topography reaches about $\sim$5 km after 6 Myrs, we also observe almost as much crustal thickening (given by the intersection of each curve with the vertical axis).
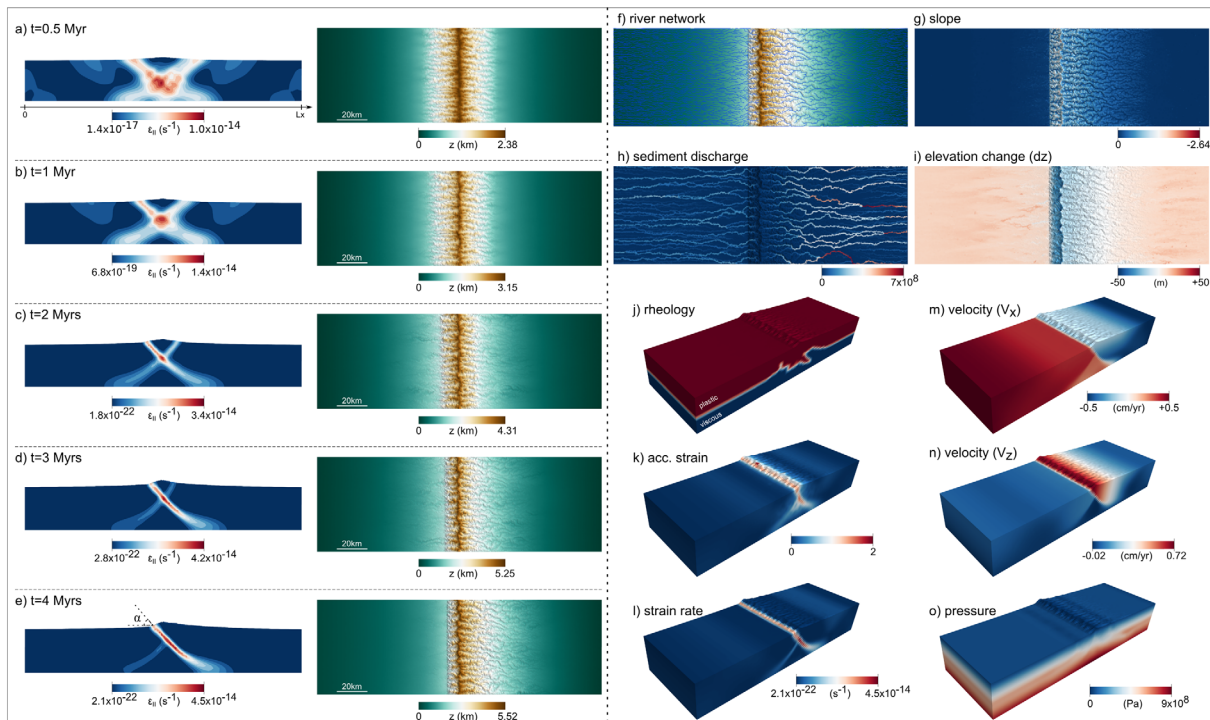
Figure 6. Reference model: (a)–(e) time evolution of the strain rate field (second invariant $\dot{\epsilon}_{II}$), as measured on the face $y = 0$ of the model, and the corresponding top view C-surface elevation z; f) river network at $t = 4$ Myrs; (g) slope measurements given by the normal of the triangles constituting the C-surface; (h) sediment discharge in m^3/yr; i) elevation change measured as the difference in elevation before and after calling Cascade, for a time step of 5 kyr; (j) pattern of dominant deformation mechanism; (k) accumulated strain; (l) strain rate; velocity field in the (m) x (V_x) and (n) z (V_z) directions; (o) dynamic pressure. Subplots (f–o) at $t = 4$ Myrs.

the K_d parameter partly controls the length of the hillslope and thus local topographic relief, K_d is probably not the most relevant parameter to investigate the influence of erosion efficiency on tectonic deformation at the scale of the entire orogen [*van der Beek and Braun*, 1998]. On the contrary, both l_f and K_f have a strong influence on landscape morphology and dynamics by controlling bedrock erodibility and climatic conditions [*Braun and Sambridge*, 1997; *Cowie et al.*, 2006; *Koons*, 2009]. For the sake of simplicity, we only vary the value of K_f relative to its reference value, and we keep K_d and l_f constant. The models that we have run and which are discussed below are summarized in Table 2.

To characterize the morphological and structural features in a quantitative manner, we define various objective measurements (Figure 7). The mean Z_{mean} and summit Z_{max} height of the orogen are measured at a given time as the mean and maximum elevation difference between the zero level and the highest (i.e., summit) node of the C-surface. The width W of the orogen is measured at the elevation $Z_{max}/2$, and the left and right half-widths are called W_L and W_R, respectively. The topographic relief of the orogen R is measured as the local maximum elevation difference along-strike the orogen (i.e., between rivers and hilltops). The asymmetry index is defined as $I_{asym} = |\frac{W_L - W_R}{W_L + W_R}|$, and tends toward 0 when the topography of the orogen is symmetric, and toward 1 when it is fully asymmetric. The dip angle of the orogen main shear zone α is defined by the dip angle of the plan that best fit the shear zone in the plastic domain.

Finally, the relative control of tectonic and surface processes on the orogen geometry and dynamics is quantified by the tectonic inward F_{in} and outward F_{out} fluxes of material and the orogen erosion E (the erosion rate measured on the orogen only, i.e., for $z > (Z_{max} - Z_{baselevel})/4$) and rock uplift rate U. The ratios F_{out}/F_{in} and E/U indicate the relevant importance of tectonics and surface processes: a ratio lower than 1 implies that tectonics dominate over surface processes, while a ratio greater than 1 implies that surface processes dominate over tectonics. These ratios also define the flux steady state condition of the topography [*Willett and Brandon*, 2002], which is obtained at the scale of the entire model for $F_{out}/F_{in} = 1$ and at the scale of the orogen only for $E/U = 1$.

Table 2. Model Parameters Used: K_f the Fluvial Erosion Coefficient, l_f the Fluvial Transport Length Scale, and K_d the Hillslope Diffusion Coefficient

Model	K_f(m.yr^{-1})	l_f(km)	K_d(m^2.yr^{-1})
Model 0	0.0	0.0	0.0
Model 1	0.001	10	0.1
Model 2	0.003	10	0.1
Model 3	0.01	10	0.1
Model 4	0.03	10	0.1
Model 5 (Ref)	0.1	10	0.1
Model 6	0.3	10	0.1

5.3. Model Descriptions at 6 Myrs

Figure 8 shows the strain rate field ($\dot{\epsilon}_{II}$) and surface topography (of the C-surface) at $t=6$ Myr for models 1–6 (i.e., models with increasing fluvial erosion efficiency K_f from 0.003 to 0.3m.yr^{-1}).

5.3.1. Model 1

When K_f is very low (Figure 8a), i.e., $K_f=0.001$m.yr^{-1}, the orogen topography is concave, with a width W of about 41 km and elevation is characterized by $Z_{mean}=4250$ m, $Z_{max}=5000$ m. Fluvial valleys are visible but do not significantly incise the topography, and the topographic relief remains small (<1000m). Deep underfilled basins are created on each side and the majority of the convergence is accommodated by thickening of the crust.

5.3.2. Model 2

When K_f is increased to 0.003m.yr^{-1} (Figure 8b), the orogen becomes more wedge-shaped: the width decreases to 36 km, while the mean and maximum elevations remain similar to those in model 1 ($Z_{mean}=4250$m, $Z_{max}=5200$m). Fluvial valleys deepen and the relief increases to about 1500 m with the increasing erosional efficiency. As in model 1, underfilled basins are created on each side and the overall thickening of the model remains very prominent.

5.3.3. Model 3

When $K_f=0.01$m.yr^{-1} (Figure 8c), the orogen width is strongly reduced ($\simeq 23$ km), and its profile is now wedge-shaped. The mean elevation is similar to that in models 1 and 2 (4250 m), whereas the relief has increased significantly to 3000 m, leading to a higher maximum elevation $Z_{max}=6500$m. Deformation is asymmetric, with a deep-rooted shear band on one side of the orogen. Underfilled basins are still present, which indicates that erosion is still limited.
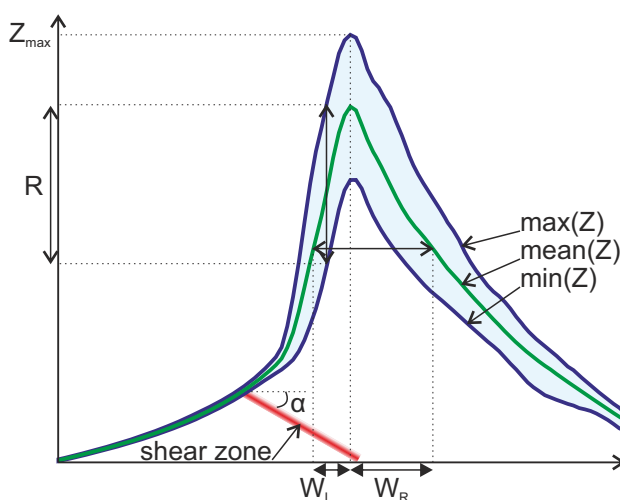
5.3.4. Model 4

For $K_f=0.03$m.yr^{-1} (Figure 8d), erosional effects are even more pronounced. The flanking basins are now fully filled, the orogen is even narrower than in model 3 ($W=21$ km), its maximum elevation has increased ($Z_{max}=6700$m), but the relief remains constant at 3000 m.

5.3.5. Model 5

For high-surface process efficiency with $K_f=0.1$m.yr^{-1}, both mean and maximum elevations are now lower ($Z_{mean}=3250$m, $Z_{max}=5250$m) than in model 4. Relief is also lower (1750 m) and the orogen width is 27 km.

5.3.6. Model 6

For a very high-surface process efficiency, with $K_f=0.3$m.yr^{-1}, the formation of topography is largely inhibited, and the orogen height is reduced to 1/3 of that in model 1 ($Z_{max}=2000$m), with a relief of about 1250 m. Significantly less thickening occurs and the shear band pattern is fully asymmetric.

A few overall qualitative observations can be made: with increasing K_f, the dip angle of the shear zones increases significantly, the width of the orogen decreases, and its asymmetry becomes more pronounced. The case without erosion exhibits a symmetric orogen similar to a pop-up structure, while cases with very efficient erosion exhibit asymmetric thrust-belt like orogens by preferentially localizing

Figure 7. Definition of the various objective measurements used to characterize the surface topography of the different models (refer to text for a description of each measurement).
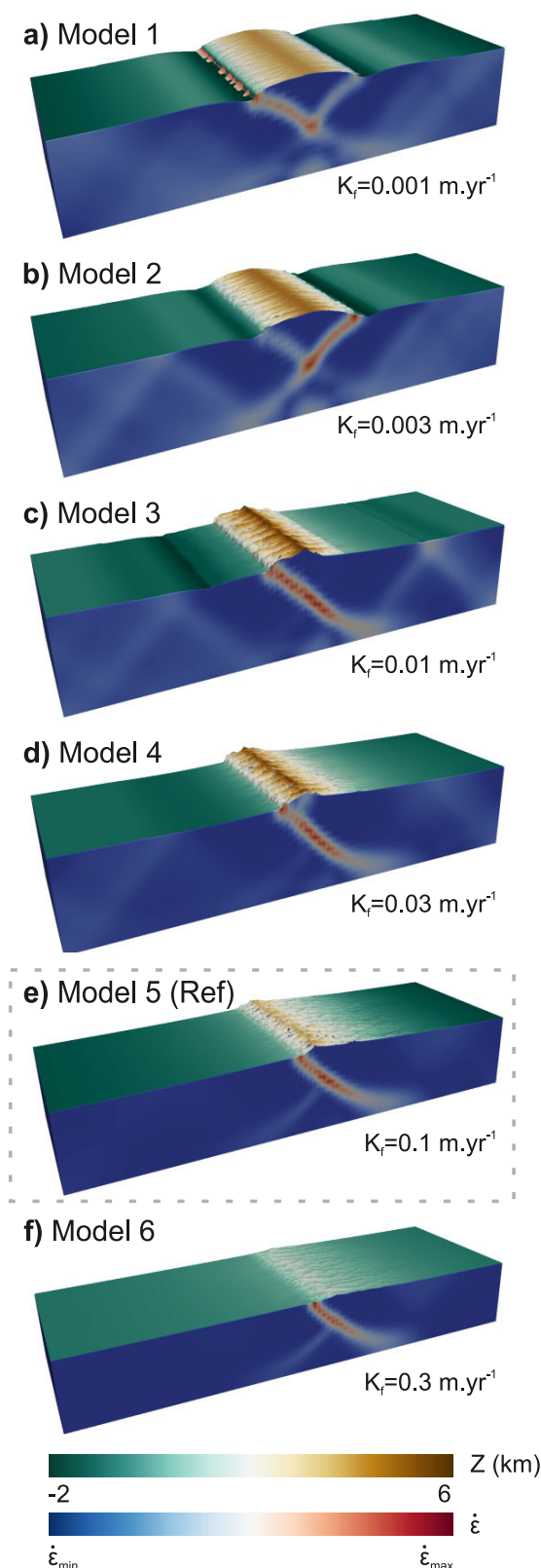
Figure 8. Strain rate field and elevation at $t = 6$ Myrs for models 1 to 6 with K_f ranging from 0.001 to 0.3 m/yr. Model 0 is not shown as it is virtually identical to model 1 without any erosional features.

strain on one active shear zone. It is important to note that the choice of the dominantly active shear zone is random. Another interesting feature of these models is the summit elevation of the surface, which seems to be a nonlinear function of erosion efficiency, as it is highest for $K_f = 0.01$ m$.yr^{-1}$ and decreases with lower or higher values.

5.4. Time Evolution

We here compare the time evolution of the models with and without surface processes. Figure 9 shows the time evolution of the objective measurements for each model.

5.4.1. Without Surface Processes

For the model without surface processes, the shear zone dip angle α increases with time from 18° to 32° at 6 Myr, while the orogen summit elevation Z_{max} increases almost linearly during the first 0.5 Myr to reach about 2 km and then increases at a lower rate to reach 5.0 km after 6 Myr. The mean elevation Z_{mean} follows a similar trend, while the width W of the orogen begins at around 43 km, then decreases during the first 2 Myr to reach 37 km and finally increases to reach 45 km after 6 Myr. Both topographic asymmetry I_{asym} and relief R remain at almost nothing. The mean orogen uplift remains approximately constant at 0.2 cm$.yr^{-1}$ during the entire simulation, which represents 20% of the total horizontal convergence rate imposed on the sides of the modeled domain.

5.4.2. With Surface Processes

Adding surface processes to the orogen significantly modifies its dynamics as well as its structural and topographic expression.

The shear zone dip angle α increases consistently with erosion efficiency and model 5 with $K_f = 0.1$ m$.yr^{-1}$ has a shear zone dip angle of 48° after 6 Myr, about 16° more than the model without surface processes. It even reaches 53° between 3 and 4 Myr, before being influenced by asymmetric deformation. Similarly, the orogen uplift rate, U, increases significantly with erosion efficiency and reaches up to 1.0cm$.yr^{-1}$ for $K_f = 0.3$cm$.yr^{-1}$. The topographic development is distinctly asymmetric after 4 Myr (asymmetry index above 0.4) for models with the highest surface process efficiency $K_f \geq 0.1$m$.yr^{-1}$, but is limited when $K_f < 0.1$m$.yr^{-1}$.

The width W of the orogen decreases with erosion efficiency, and the reference model orogen (model 5) is about 20–25 km narrower than the model with little or no surface processes after 6

Myr. In contrast, the mean elevation, Z_{mean}, remains approximately constant for cases with $K_f \leq 0.03 \mathrm{m.yr}^{-1}$ but decreases significantly when K_f is greater. The orogen maximum elevation behaves as a nonlinear function of erosion efficiency. When increasing K_f, Z_{max} first increases from 5 to 6.5 km for models 0 to 4 ($K_f \leq 0.03 \mathrm{m.yr}^{-1}$) and then decreases from 6.5 to almost 2 km for models 4 to 6 ($K_f \geq 0.03 \mathrm{m.yr}^{-1}$). This behavior is directly related to relief development, which, by definition, sets the difference between mean and maximum elevation. Indeed, the topographic relief R increases with K_f for models with $K_f \leq 0.03 \mathrm{m.yr}^{-1}$ and then decreases for $K_f \geq 0.03 \mathrm{m.yr}^{-1}$.

This nonlinear relationship between relief R or summit elevation Z_{max} and K_f is related to the steady state of the topography. Only the two models with the highest erosion efficiency ($K_f > 0.03 \mathrm{m.yr}^{-1}$) develop a topography close to flux steady state condition at the scale of the orogen ($E/U=1$), and only model 6 with $K_f=0.3 \mathrm{m.yr}^{-1}$ reaches it at the scale of the entire model ($F_{out}/F_{in}=1$).

6. Discussion

6.1. Tectonic Controls
We first discuss the main tectonic controls in the absence of surface processes.

6.1.1. Shear Zone Angle
In Model 0, the shear zone dip angle α increases almost linearly with time (Figure 9). This is a consequence of (1) strain-weakening, which increases the static optimal dip angle of the frictional-plastic part of the shear zone (i.e., $45^\circ - \phi/2$) from 37.5° ($\phi=15^\circ$) to 44° ($\phi^{sw}=2^\circ$), and (2) the advection of shear zones toward each other, which tends to rotate their planes toward the vertical direction. These two effects are strongly dependent on strain weakening, as without strain-weakening only transient shear bands would be promoted.

6.1.2. Orogen Width and Uplift Rate
Assuming that the orogen is bounded at startup by two shear bands that intersect at a depth d and that make an angle α with the vertical, the initial width of the orogen is given by $2d\tan\alpha$, which in our case (taking $d \simeq 14 \mathrm{km}$ and $\alpha \simeq \pi/4 + \phi/2^\circ$) yields a width of approximately 36 km, i.e., 1/5 of the length of the model (e.g., Figure 6a).

The combined effect of strain-weakening and shear zone advection explain why the width W of the orogen decreases with time at the beginning of the model simulation, but does not account for why it later increases. The dynamics of the orogen is mainly controlled by frictional-plastic deformation along the shear zones, which tends to uplift the orogen and narrow it as α increases, but which, also, by viscous deformation in response to the topographic load, tends to widen and subside the orogen. During the first 2 Myr of the simulation, orogen narrowing results from progressive steepening of the shear zones, while during the last 3 Myr, widening of the orogen is induced by the viscous flow resulting from topographic loading. In addition, flattening of the shear zone toward the surface, owing to stress rotation resulting from the topographic loading [*Braun and Yamato*, 2010], also favors the widening of the orogen with topographic development.

6.1.3. Strain Localization
The localization of deformation seems limited, as the orogen average rock uplift rate ($0.2 \mathrm{cm.yr}^{-1}$) represents only 20% of the total horizontal convergence rate ($1 \mathrm{cm.yr}^{-1}$), and the orogen uplift flux (i.e., the rock uplift rate times the surface area of the orogen) corresponds to approximately 30% of the convergence flux. This indicates that a large part of the convergence is accommodated by diffuse distributed deformation leading to an overall thickening of the crust. About 50% of the material that enters the domain through the boundaries is viscous crust and by definition does not lead to localized deformation and thus does not contribute to relief growth. The orogen uplift flux corresponds to approximately 60% of the brittle crust convergence flux.

6.1.4. Orogen Elevation
The most significant effect of tectonic deformation on the surface expression of the orogen concerns its elevation. Both the mean (Z_{mean}) and the maximum (Z_{max}) elevation increase almost linearly with time, except for the first 0.5 Myr during the initiation of the orogen.

6.2. Influence of Surface Process Efficiency on Orogen Dynamics
The morphology of the orogen in our models is mainly governed by three components: (1) the tectonic convergence velocity at the lateral sides of the model; (2) the efficiency of strain localization on the orogen
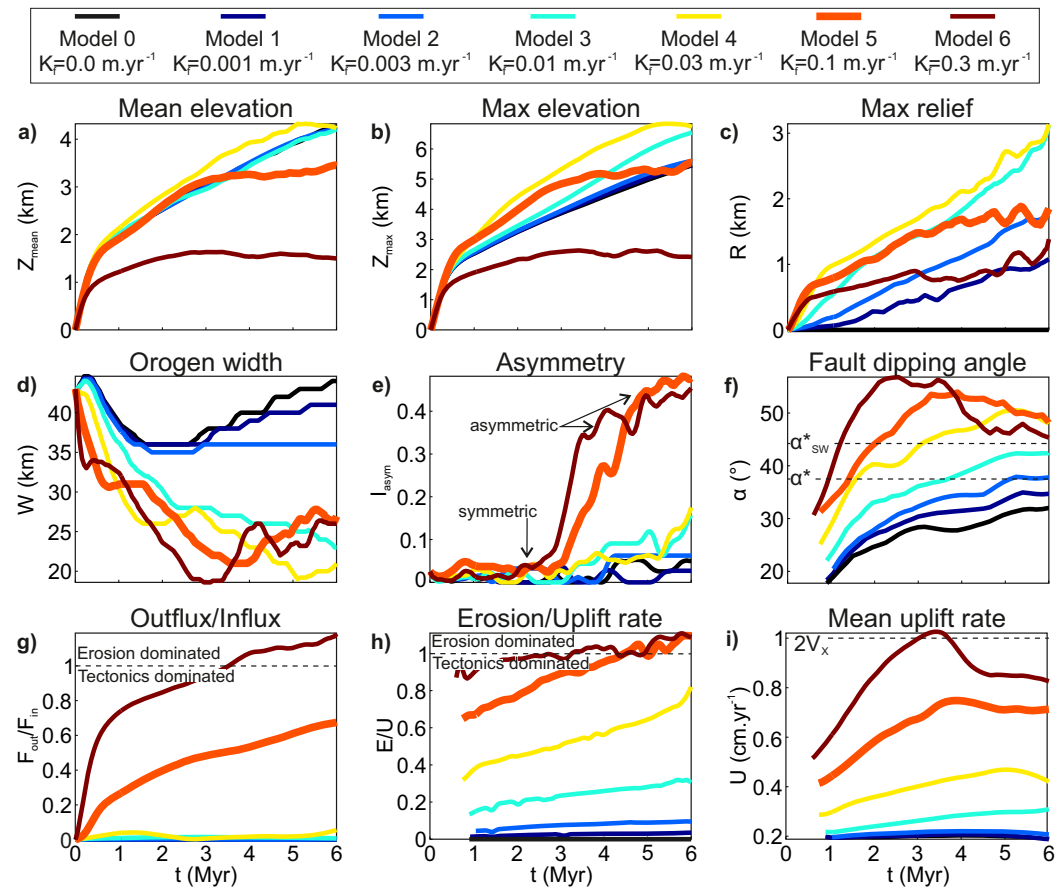
Figure 9. Time evolution of the objective measurements characterizing the topographic, structural, and dynamic expressions of the orogen: (a) Z_{mean} the mean orogen elevation; (b) Z_{max} the maximum elevation; (c) R the local relief; (d) W the orogen width; (e) I_{asym} the topographic asymmetry; (f) α the shear zone dip angle (the starred values represent the Coulomb angle values before and after strain weakening); (g) F_{out}/F_{in} the ratio of outward on inward material fluxes; (h) E/U the mean ratio of orogen erosion to uplift; and (i) U the mean orogen uplift.

shear zones that allows the orogen to convert the boundary convergent velocity into an orogenic uplift U; and (3) the erosion efficiency K_f, which controls the orogen erosion rate E, the sedimentary outflux F_{out} and the local relief R.

6.2.1. Shear Zone Angle
The shear zone angle α increases consistently with the erosion efficiency K_f (Figure 9f). We attribute this to the erosional unloading of the orogen, which results in a decrease of the pressure and of the normal stress on the shear zone but also in an increase of its tangential stress, thus favoring localization of strain and steepening of the shear zones. In case of very high erosion efficiency, the transition between symmetric and asymmetric modes leads to a change of the dip angle. We attribute this to the reorganization of topography, from a symmetric toward an asymmetric one, which leads to higher vertical stresses on the remaining active shear zone. This induces stress rotation owing from the topographic load *Braun and Yamato* [2010], and a flattening of the shear zone toward the surface.

6.2.2. Orogen Width and Uplift Rate
The progressive steepening of the shear zones with increasing surface process efficiency results in a reduction of the orogen width W and verticalizes the velocity flow field at the surface. In turn, the increased erosional flux in a narrower orogenic domain leads to an increase of the rock uplift rate U. The erosional efficiency therefore has a positive effect, through the shear zone dip angle α and the orogen width W, on the orogen uplift rate U. This is interesting as it illustrates that convergence rate alone does not explain the

orogen uplift rate, and that surface processes, as well as the thermomechanical state of the crust, must be taken into account [*Koons*, 1990; *Willett et al.*, 1993; *Beaumont et al.*, 2004, 2006; *Koons et al.*, 2010].

6.2.3. Orogen Asymmetry

Topographic and structural asymmetry develops naturally in the models without imposing asymmetric boundary conditions, as is quite commonly done in geodynamic numerical models [*Beaumont et al.*, 1992; *Willett*, 1999; *Braun and Yamato*, 2010]. In the models presented here, orogen asymmetry I_{asym} develops as a consequence of preferential strain weakening of one shear zone [e.g., *Huismans et al.*, 2005]. The model results indicate a positive feedback of increasing erosion efficiency K_f on the development of strain localization and asymmetry. As already illustrated, strain localization by favoring advection of the shear zones toward each other leads to an increase of their dip angle α, which makes them mechanically inefficient for accommodating further convergence. This results in a mechanically unstable settings that ultimately leads to the abandonment of one shear zone and the subsequent development of asymmetry. The onset of strain weakening and the development of asymmetric localized deformation occur in models 5 and 6 around 3 Myr. This affects the dip angle α that decreases, the orogen width W that increases, and the orogen averaged rock uplift U, which decreases (see Figure 9).

6.2.4. Local Topographic Relief

Evolution of the local topographic relief offers insights into the dynamics of topography above the main rivers, especially during the transient response to tectonic or erosional perturbation. Our results indicate a nonlinear relationship between erosion efficiency K_f and the local topographic relief R, which is largest for $K_f = 0.03 \text{m.yr}^{-1}$ and decreases with lower or higher values of K_f. However, from a derivation of steady state orogen morphology (see Appendix B), R should decrease when increasing K_f. It is therefore important to note that most of the models presented here have not reached steady state at the end of the simulation, except the models with $K_f > 0.03 \text{m.yr}^{-1}$. These latter models have R that decreases with K_f, consistent with steady state predictions. On the contrary, models which are far from a steady state condition have R that increases with K_f. We attribute this behavior to the increase with K_f of the rate of local relief production by fluvial incision during transient conditions (i.e., nonsteady).

6.2.5. Summit Elevation

The explanation is more complex for Z_{max}, as it depends both on the orogen width W, which sets the potential maximum elevation of the orogen, and on the local relief R. Therefore at steady state, summit elevation Z_{max} is expected to decrease with erosion efficiency K_f, as it has a negative effect on both the orogen width W and the local relief R. However, our results indicate a nonlinear relationship between erosion efficiency K_f and summit elevation Z_{max}. As expected, summit elevation Z_{max} of models at steady state ($K_f > 0.03 \text{m.yr}^{-1}$) decreases with K_f. On the contrary, summit elevation Z_{max} increases with K_f for models that did not reach steady state ($K_f \leq 0.03 \text{m.yr}^{-1}$).

The increase of the rate of relief production during transient conditions with increasing K_f also results in the surface uplift of summits by isostatic compensation. While during steady state conditions, surface uplift is roughly compensated by erosion, even for the summits [*Koons et al.*, 2002]. It is particularly remarkable that in our models, orogens submitted to surface processes can develop higher summits during transient conditions than orogen without surface processes, which highlights the importance and the complexity of the feedback between surface processes and tectonics during orogeny.

6.3. First-Order Control of Along-Strike Erosion Efficiency Gradients

Despite their 3-D formalism, the models presented in this study are more representative of 2-D than 3-D physical systems due to their boundary conditions. On Earth, two-dimensional (i.e., cylindrical) convergence zones are the exception rather than the norm and most orogens involve a nonnegligible along-strike component. However, modeling real 3-D tectonic settings, such as oblique orogens, is challenging as it involves consistent boundary conditions in the three dimensions of space. Because of the no-flux boundary conditions imposed on the sides of both the FANTOM and Cascade models, extending our approach to a real 3-D tectonic setup is beyond the scope of this paper. However, using the same tectonic setup, we can investigate the influence of an along-strike gradient of precipitation on the 3-D distribution of deformation and surface morphology of the orogen. We have therefore defined a linearly varying coefficient of erosion efficiency K_f between the two lateral walls, with $K_f = 0.01 \text{m.yr}^{-1}$ in $y = 0$ (i.e., dry side) and $K_f = 0.1 \text{m.yr}^{-1}$ (i.e., wet side) in $y = L_y$, while keeping all other parameters unchanged.
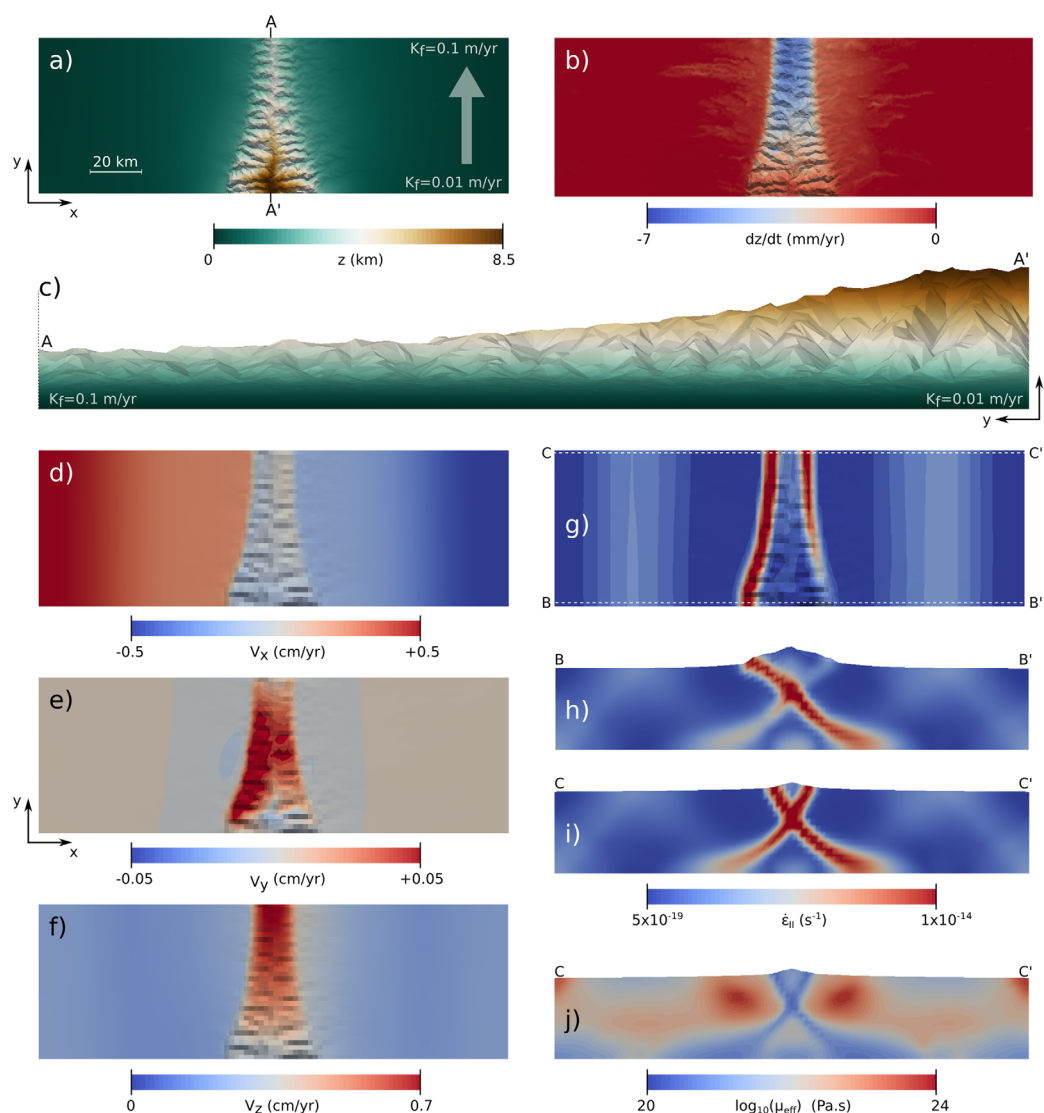
Figure 10. Model with linear gradient of erosion efficiency K_f at $t = 5$ Myrs. (a) C-surface elevation z; (b) erosion rate; (c) cross section of the orogen along strike; (d,e,f) top view of $x-$, $y-$ and $z-$ velocity components; (g,h,i) top view of strain rate field and associated cross sections AA' and BB'; (j) Effective viscosity along BB' cross section.

Results at 5 Myrs are shown in Figure 10 and clearly show the 3-D characteristics of this model compared to the previous ones. Indeed, the maximum elevation of the orogen varies along-strike between 4 and 8.5 km, with the highest elevation obtained on the dry side of the model (Figure 10a). The width of the orogen is also 2 times greater on the dry side of the model, 30 km, than on the wet side. These results are consistent with the along-strike gradient of K_f and with the results obtained with the previous models using $K_f = 0.01$ or 0.1 m.yr^{-1}. Erosion rates reach up 7mm.yr^{-1} on the wet side of the model, which is about 10 times greater than on the dry side (Figure 10b). The $x-$, $y-$, and $z-$ components of the velocity field are shown in Figures 10d, 10e, and 10f. The rock uplift rate (i.e., V_z) shows much higher values (7mm.yr^{-1}) on the wet side of the model, where the orogen is narrow, than on the dry side, where the orogen is wider ($\sim$3mm.yr^{-1}). It is also interesting to note that the wet side of the orogen has almost reached a dynamic equilibrium state while the dry side is still building topography as its uplift rate is greater than its erosion rate. Quite remarkably the along-strike component of the velocity (i.e., V_y) takes values of about 0.05cm. yr^{-1} in the orogen, which indicates a tectonic flux of material from the dry to wet side of the model. This flux of material occurs mainly in the upper part of the crust, which is weak as it displays low effective viscosity (Figure 10j), and is driven by the along-strike gradient of potential energy that emerges in response to the gradient of erosion efficiency K_f. Accordingly, the wet side of the orogen, by eroding efficiently, offers a
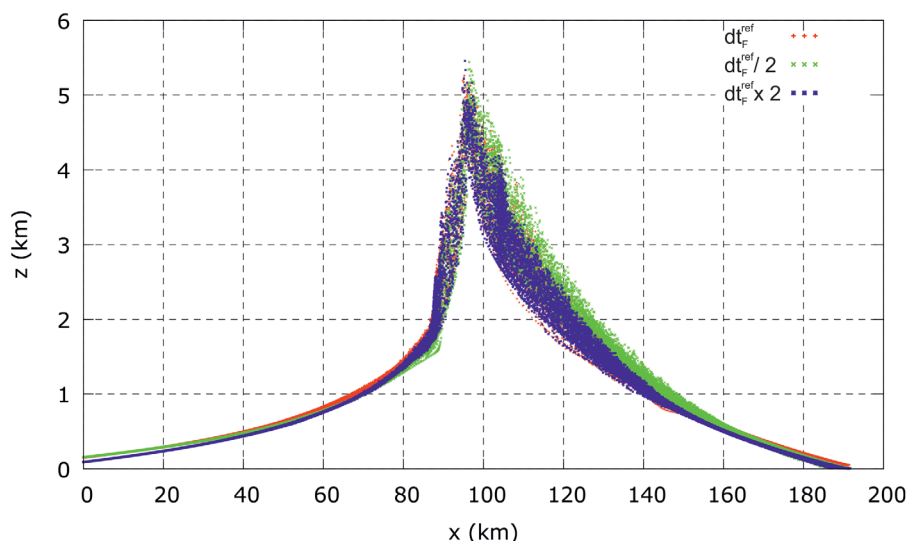
Figure 11. Swath profiles of the *C*-surface at *t* = 5 Myr in the case where three different tectonic time steps have been used: $\delta t_F = 5000$ yr, half this value ($\delta t_F = 2500$ yr) and twice this value ($\delta t_F = 10000$ yr). In all three cases the Cascade time step remained constant at $\delta t_C = 10$ yr.

suitable exit path to the orogen material stressed by both across-strike tectonic forces and along-strike gravitational forces. The strain rate (Figures 10g, 10h, and 10i) shows that the structural response of the system to the gradient of erosion efficiency is the development of oblique shear zones relative to *x*, the main convergence direction, due to the effective dependance of the dip angle to K_f. These oblique shear zones accommodate both the across-strike imposed convergence and the emerging lateral flux of material, leading to a strike-component in its strain field.

This illustrative model clearly demonstrates the potential of using the FANTOM model to investigate the dynamics of tectonic deformation and landscape evolution in settings with a 3-D component. Even if mainly illustrative, this model could also offers some insights on the role of a lateral gradient of precipitation or erosion efficiency on the dynamics of orogens, as it occurs, for example, along the Andes [e.g., *Montgomery et al.*, 2001].

6.4. Model Limitations

We have tested the sensitivity of orogen dynamics to fluvial surface process efficiency by varying K_f, which includes both the effect of precipitation and erodibility. The limitations of our approach relate to limitations in the surface process model, the tectonic model, and the model setup.

The surface process model Cascade does not properly reproduce the "tool and cover" effect exerted by the sediment load on fluvial incision [*Sklar and Dietrich*, 2004; *Turowski et al.*, 2007]. In Cascade, high sediment load (i.e., close to or at capacity) leads to low or null incision rate, consistent with the sediment "cover" effect, whereas, the greatest incision rate is predicted for the lowest sediment load (i.e., at undercapacity). The sediment "tool" effect is expected to lead to the greatest incision rate for intermediate sediment load [*Sklar and Dietrich*, 2004; *Turowski et al.*, 2007]. In addition, Cascade is based on the assumption that the incision rate can be modeled using the concept of a river dominant "effective" water discharge. It is well established that the stochastic distribution of water discharge has a strong influence on the dynamics of the fluvial incision law [*Molnar*, 2001; *Tucker and Bras*, 2000; *Lague et al.*, 2005]. In particular, the linear dependence of the incision rate on the topographic slope, as used in Cascade, is inconsistent with highly variable climatic conditions [*Lague et al.*, 2005]. The effects of these highly nonlinear effects that could possibly lead to different couplings between surface processes and tectonics need to be investigated in future studies but are beyond the scope of the present work.

The tectonic model, although solving for large deformation flows, is limited to about 2 million degrees of freedom [*Thieulot*, 2011]. To allow for reasonable mesh resolution in the vicinity of the free surface, we had to limit the model domain to crustal scale. Solving for large deformation flows in 3-D is an inherently challenging problem for which no readymade recipe exists. The models presented here show significant

progress; however, if compared with the existing literature. With respect to these computational limitations, the tectonic model was limited to crustal scale to allow for a mesh resolution of approximately 2 km. Owing to the absence of the underlying lithospheric and sublithosperic mantle, the model setup does not allow the formation of a deep crustal root and isostasy is maintained mainly by stresses associated with viscous flow in the lower crust. The model results can therefore be understood in the context of orogens that are supported by viscous flow rather than by local or regional isostatic conditions. The tectonic model is deliberately simple and a more systematic study of the influence of rheology, thermal state (initial geotherm and radiogenic heat production), and boundary conditions is warranted.

7. Conclusions

We present a new forward numerical model that couples 3-D tectonic deformation and surface processes. The transfer of information between the tectonic and the surface process model is ensured by the use of an appropriate algorithm that includes: (1) the use of different time stepping and spatial discretization for the tectonic and surface process model; (2) an adaptive irregular grid for the surface process model that allows surface advection by tectonic deformation; and (3) local interpolation filters to transfer information between the two grids. The 3-D numerical model was used to study the influence of surface process efficiency on orogeny. The model results demonstrate that the structural style and dynamics of mountain building are strongly sensitive to surface process efficiency.

We conclude the following:

1. the localization of deformation increases as a function of erosion efficiency;
2. the fault dip angle is the result of a complex interplay between asymmetric or symmetric structural geometry, tectonics, and erosion efficiency: in this work, we observe that increasing the erosion efficiency leads to a steepening of the fault dip angle;
3. surface processes favor both the narrowing of the orogen and the localization of deformation on the orogen shear zones, which leads to an increase of rock uplift (and in turn of erosion rates);
4. the lower the erosion efficiency, the longer it will take to reach steady state elevation and relief;
5. the coupling between tectonic deformation and surface processes promotes an increase of orogen summit elevation with erosion efficiency during nonsteady state conditions.
6. orogen asymmetry is enhanced by the erosion efficiency through a strain-weakening feedback mechanism;

We believe these model results represent a first step toward identification of the signature of surface processes in intracontinental orogens, and more generally, in areas of tectonic compression.

Appendix A: Resolution and Time Steps

Starting from the model domain length L_x and a given element number in the $x-$direction $ncellx$, the Finite Element grid spacing is given by $dx = L_x/ncellx$. In our case, the spatial resolution in FANTOM is then $dx = 2$ km. This, in turn, sets the minimum resolution of the C-surface, as it is desirable to have at least one Cascade point per element. We start with a minimum of only 4 points per element (at $t = 0$), as due to the advection of the surface towards the orogen, the C-surface point density increases 10-fold (from 4 to 40). While many more points would have allowed us to better represent the C-surface, (1) the Cascade model does not represent the physics of surface processes at a resolution finer than 10–100 m. (2) their effect on the tectonic model would in any case be smoothed out by the moving least square algorithm used for the interpolation; (3) it would have been at the cost of a dramatic increase in computational time spent in Cascade (δt_C is bound by a strict Courant condition).

In the reference model, the tectonic time step is set to a constant value $\delta t_F = 5000$ year, which corresponds to a Courant number $C \simeq 0.01$. The reference model was additionally run at half the reference tectonic time step and twice the reference tectonic time step in order to assess whether it influences the outcome of the simulation (while keeping the Cascade time step δt_C set to 10 year). Looking at the swath profiles of the three recovered C-surfaces at $t = 5$ Myrs as shown in Figure 11, one sees that these coincide within a 50–100 m interval, well within what is expected as both initial accumulated strain region and C-surface layout are distributed at random.

Appendix B: Morphologic Characteristics at Steady State

Let us consider the case of a river that is at steady state, with its erosion rate E equal to the rock uplift rate U. Under these conditions, it can be demonstrated that $q_s = UAb$ by integrating the product of erosion over the drainage area and by assuming that a fraction $b \leq 1$ of the sediment load exerts the main control on the river slope [*Cowie et al.*, 2006]. We can then derive from equation (14) the slope of the river at steady state ($\partial h / \partial t = 0$):

$$S = \frac{U}{K_f}\left(b + \frac{w_f l_f}{A}\right) \tag{B1}$$

The drainage area at the river head A_0 is also a useful landscape metric to characterize the horizontal spacing of rivers, the hillslope elevation, and the local topographic relief [e.g., *Whipple and Tucker*, 1999; *Tucker and Whipple*, 2002]. If we assume that the slope S_0 of the river at the channel head is equal to a constant, such as the angle of respose of the hillslope slope, which is a convenient but rough approximation for hillslope controlled by diffusion (equation (16)), then we obtain:

$$A_0 = w_f l_f \left(\frac{K_f S_0}{U} - b\right)^{-1} \tag{B2}$$

Now, because we are interested in analysing the effect of varying K_f on the landscape morphology, we can compare the effect of an increment of erosion efficiency ΔK_f on the variation of the channel head area Δ_0, assuming that all the other parameters remain constant:

$$\Delta A_0 = \frac{w_f l_f U}{S_0} \frac{1}{\Delta K_f} \tag{B3}$$

A significant outcome of this relation is that the variation of the river head drainage area scales in inverse proportion to the variation of erosion efficiency. Therefore, we can also expect the local topographic relief and the river horizontal spacing, which both scale with the square root of A_0, to increase with K_f.

References

Allken, V., R. S. Huismans, and C. Thieulot (2011), Three-dimensional numerical modeling of upper crustal extensional systems, *J. Geophys. Res.*, *116*, B10409, doi:10.1029/2011JB008319.

Allken, V., R. S. Huismans, and C. Thieulot (2012), Factors controlling the mode of rift interaction in brittle-ductile coupled systems: A 3D numerical study, *Geochem. Geophys. Geosyst.*, *13*, Q05010, doi:10.1029/2012GC004077.

Avouac, J. P., and E. B. Burov (1996), Erosion as a driving mechanism of intracontinental mountain growth, *J. Geophys. Res.*, *101*(B8), 17,747–17,769.

Batt, G. E., and J. Braun (1997), On the thermomechanical evolution of compressional orogens, *Geophys. J. Int.*, *128*, 364–382.

Batt, G. E., and J. Braun (1999), The tectonic evolution of the Southern Alps, New Zealand: Insights from fully thermally coupled dynamical modelling, *Geophys. J. Int.*, *136*, 403–420.

Beaumont, C., P. Fullsack, and J. Hamilton (1992), Erosional control of active compressional orogens, in *Thrust Tectonics*, edited by K. R. McClay, pp. 1–18, Chapman and Hall, New York.

Beaumont, C., P. J. J. Kamp, J. Hamilton, and P. Fullsack (1996), The continental collision zone, South Island, New Zealand: Comparison of geodynamical models and observations, *J. Geophys. Res.*, *101*(B2), 3333–3359.

Beaumont, C., R. A. Jamieson, M. H. Nguyen, and S. Medvedev (2004), Crustal channel flows: 1. Numerical models with applications to the tectonics of the Himalayan-Tibetan orogen, *J. Geophys. Res.*, *109*, B06406, doi:10.1029/2003JB002809.

Beaumont, C., M. H. Nguyen, R. A. Jamieson, and S. Ellis (2006), Crustal flow modes in large hot orogens, in Channel Flow, Ductile Extrusion and Exhumation in Continental Collision Zones, edited by R. D. Law, M. P. Searle, and L. Godin, *Geol. Soc. Spec. Publ.*, *268*, 91–145.

Braun, J. (2006), Recent advances and current problems in modelling surface processes and their interaction with crustal deformation, in Analogue and Numerical Modelling of Crustal-Scale Processes, *Geol. Soc. Spec. Publ.*, *253*, 307–325.

Braun, J. (2010), The many surface expressions of mantle dynamics, *Nat. Geosci.*, *3*, 825–833, doi:10.1038/ngeo1020.

Braun, J., and M. Sambridge (1997), Modelling landscape evolution on geological time scales: A new method based on irregular spatial discretisation, *Basin Res.*, *9*, 27–52.

Braun, J., and R. Shaw (2001), A thin-plate model of Palaeozoic deformation of the Australian lithosphere: Implications for understanding the dynamics of intracratonic deformation, *Geol. Soc. Spec. Publ.*, *184*, 165–193, doi:10.1144/GSL.SP.2001.184.01.09.

Braun, J., and S. D. Willett (2013), A very efficient $O(n)$, implicit and parallel method to solve the stream power equation governing fluvial incision and landscape evolution, *Geomorphology*, *180–181*, 170–179.

Braun, J., and P. Yamato (2010), Structural evolution of a three-dimensional, finite-width crust wedge, *Tectonophysics*, *484*, 181–192, doi:10.1016/j.tecto.2009.08.032.

Braun, J., C. Thieulot, Ph. Fullsack, M. DeKool, C. Beaumont and R. Huismans (2008), DOUAR: A new three-dimensional creeping flow numerical model for the solution of geological problems, *Phys. Earth Planet. Inter.*, *171*, 76–91.

Burbank, D. W., J. Leland, E. Fielding, R. S. Anderson, N. Brozovic, M. R. Reid, and C. Duncan (1996), Bedrock incision, rock uplift and threshold hillslopes in the northwestern Himalayas, *Nature*, *379*, 505–510, doi:10.1038/379505a0.

Burov, E., and S. Cloetingh (1997), Erosion and rift dynamics: New thermomechanical aspects of post-rift evolution of extensional basins, *Earth Planet. Sci. Lett.*, *150*, 7–26.

Burov, E., and A. Poliakov (2001), Erosion and rheology controls on synrift and postrift evolution: Verifying old and new ideas using a fully coupled numerical model, *J. Geophys. Res.*, *106*(B8), 16,461–16,481.

Burov, E., and G. Toussaint (2007), Surface processes and tectonics: Forcing of continental subduction and deep processes, *Global Planet. Change*, *58*, 141–164.

Castelltort, S., L. Goren, S. D. Willett, J.-D. Champagnac, F. Herman, and J. Braun (2012), River drainage patterns in the New Zealand Alps primarily controlled by plate tectonic strain, *Nat. Geosci.*, *5*, 744–748, doi:10.1038/ngeo1582.

Collignon, M., B. J. P. Kaus, D. A. May, and N. Fernandez (2014), Influences of surface processes on fold growth during 3-D detachment folding, *Geochem. Geophys. Geosyst. 15*, 3281–3303, doi:10.1002/2014GC005450.

Coulthard, T. J. (2001), Landscape evolution models: A software review, *Hydrol. Processes*, *15*, 165–173.

Cowie, P. A., M. Attal, G. E. Tucker, A. C. Whittaker, M. Naylor, A. Ganas, and G. P. Roberts (2006), Investigating the surface process response to fault interaction and linkage using a numerical modelling approach, *Basin Res.*, *18*, 231–266, doi:10.1111/j.1365-2117.2006.00298.x.

Crave, A., and P. Davy (2001), A stochastic ''precipiton'' model for simulating erosion/sedimentation dynamics, *Comput. Geosci.*, *27*, 815–827.

Croissant, T., and J. Braun (2014), Constraining the stream power law: A novel approach combining a landscape evolution model and an inversion method, *Earth Surf. Dyn.*, *2*, 155–166, doi:10.5194/esurf-2-155-2014.

Dahlen, F. A. (1990), Critical taper model of fold-and-thrust belts and accretionary wedges, *Annu. Rev. Earth Planet. Sci.*, *18*, 55–99.

Dahlen, F. A., J. Suppe, and D. Davis (1984), Mechanics of fold-and-thrust belts and accretionary wedges: Cohesive Coulomb theory, *J. Geophys. Res.*, *89*(B12), 10,087–10,101.

Davy, P., and D. Lague (2009), Fluvial erosion/transport equation of landscape evolution models revisited, *J. Geophys. Res.*, *114*, F03007, doi: 10.1029/2008JF001146.

Erdős, Z., R. S. Huismans, P. van der Beek, and C. Thieulot (2014), Extensional inheritance and surface processes as controlling factors of mountain belt structure, *J. Geophys. Res.*, doi:10.1002/2014JB011408, in press.

Fischer, K. D., T. Jahr, and G. Jentzsch (2004), Evolution of the Variscan foreland-basin: Modelling the interactions between tectonics and surface processes, *Phys. Chem. Earth*, *29*, 665–671, doi:10.1016/j.pce.2004.03.004.

Fullsack, P. (1995), An arbitrary Lagrangian-Eulerian formulation for creeping flows and its application in tectonic models, *Geophys. J. Int.*, *120*, 1–23.

Garcia-Castellanos, D. (2002), Interplay between lithospheric flexure and river transport in foreland basins, *Basin Res.*, *14*, 89–104.

Garcia-Castellanos, D., M. Fernández, and M. Torne (1997), Numerical modeling of Foreland Basin Formation: A program relating thrusting, flexure, sediment geometry and lithosphere rheology, *Comput. Geosci.*, *23*, 993–1003.

Gerbault, M., S. Henrys, and F. Davey (2003), Numerical models of lithospheric deformation forming the Southern Alps of New Zealand, *J. Geophys. Res.*, *14*, 89–104.

Godard, V., R. Cattin, and J. Lavé (2004), Numerical modeling of mountain building: Interplay between erosion law and crustal rheology, *Geophys. Res. Lett.*, *31*, L23607, doi:10.1029/2004GL021006.

Godard, V., J. Lavé, and R. Cattin (2006), Numerical modelling of erosion processes in the Himalayas of Nepal: Effects of spatial variations of rock strength and precipitation, in Analogue and Numerical Modelling of Crustal-Scale Processes, *Geol. Soc. Spec. Publ.*, *253*(1), 341–358.

Graveleau, F., J.-E. Hurtrez, S. Dominguez, and J. Malavieille (2011), A new experimental material for modeling relief dynamics and interactions between tectonics and surface processes, *Tectonophysics*, *513*, 68–87.

Gupta, A. (2000a), *WSMP: Watson Sparse Matrix Package (Part-I: Direct solution of Symmetric Sparse Systems)*, Tech. Rep. RC 21888, IBM T. J. Watson Res. Cent., York town Heights, N. Y., November 2000. [Available at http://www.research.ibm.com/projects/wsmp.]

Gupta, A. (2000b), *WSMP: Watson Sparse Matrix Package (Part-II: Direct Solution of General Systems)*, Tech. Rep. RC 24398, IBM T. J. Watson Res. Cent., York town Heights, N. Y., November 2007. [Available at http://www.research.ibm.com/projects/wsmp.]

Hilley, G. E., and M. R. Strecker (2004), Steady state erosion of critical Coulomb wedges with applications to Taiwan and the Himalaya, *J. Geophys. Res.*, *109*, B01411, doi:10.1029/2002JB002284.

Huismans, R. S. and C. Beaumont (2007), Roles of lithospheric strain softening and heterogeneity in determining the geometry of rifts and continental margins, in G. D. Karner, G. Manatschal, and L. M. Pinheiro, Imaging, Mapping and Modelling Continental Lithosphere Extension and Breakup, *Geol. Soc. Spec. Publ.*, *282*, 111–138, doi:10.1144/SP282.6.

Huismans, R. S., S. J. H. Buiter, and C. Beaumont (2005), Effect of plastic-viscous layering and strain softening on mode selection during lithospheric extension, *J. Geophys. Res.*, *110*, B02406, doi:10.1029/2004JB003114.

Iaffaldano, G., H.-P. Bunge, and T. H. Dixon (2006), Feedback between mountain belt growth and plate convergence, *Geology*, *34*, 893–896, doi:10.1130/G22661.1.

Iaffaldano, G., L. Husson, and H.-P. Bunge (2011), Monsoon speeds up Indian plate motion, *Earth Planet. Sci. Lett.*, *304*, 503–510.

Kaus, B. J. P., C. Steedman, and T.W. Becker (2008), From passive continental margin to mountain belt: Insights from analytical and numerical models and application to Taiwan, *Phys. Earth Planet. Inter.*, *171*, 235–251.

Kooi, H., and C. Beaumont (1994), Escarpment evolution on high-elevation rifted margins: Insights derived from a surface processes model that combines diffusion, advection, and reaction, *J. Geophys. Res.*, *99*(B6), 12,191–12,209.

Koons, P. O. (1990), Two-sided orogen: Collision and erosion from the sandbox to the Southern Alps, New Zealand, *Geology*, *18*, 679–682.

Koons, P. O. (1994), Three-dimensional critical wedges: Tectonics and topography in oblique collisional orogens, *J. Geophys. Res.*, *99*, 12,301–12,315.

Koons, P. O. (1998), Modeling the topographic evolution of collisional belts, *Annu. Rev. Earth Planet. Sci.*, *23*, 375–408.

Koons, P. O. (2009), On the implications of low spatial correlation of tectonic and climate variables in the western European Alps, *Geology*, *37*, 863–864, doi:10.1130/focus092009.1.

Koons, P. O., P. K. Zeitler, C. P. Chamberlain, D. Craw, and A. S. Meltzer (2002), Mechanical links between erosion and metamorphism in Nanga Parbat, Pakistan Himalaya, *Am. J. Sci.*, *302*, 749–773.

Koons, P. O., B. P. Hooks, T. Pavlis, P. Upton, and A. D. Barker (2010), Three-dimensional mechanics of Yakutat convergence in the southern Alaskan plate corner, *Tectonics*, *29*, TC4008, doi:10.1029/2009TC002463.

Kurfess, D., and O. Heidbach (2009), CASQUS: A new simulation tool for coupled 3D finite element modeling of tectonic and surface processes based on ABAQUS^{TM} and Cascade, *Comput. Geosci.*, *35*, 1959–1967.

Lague, D., N. Hovius, and P. Davy (2005), Discharge, discharge variability, and the bedrock channel profile, *J. Geophys. Res.*, *110*, F04006, doi:10.1029/2004JF000259.

Lavé, J. (2005), Analytic solution of the mean elevation of a watershed dominated by fluvial incision and hillslope landslides, *Geophys. Res. Lett.*, *32*, L11403, doi:10.1029/2005GL022482.

Leopold, L. B., and T. Maddock (1953), The hydraulic geometry of stream channels and some physiographic implications, *Geol. Surv. Prof. Pap.*, *252*. [Available at: http://eps.berkeley.edu/people/lunaleopold/%28040%29%20The%20Hydraulic%20Geometry%20of%20-Stream%20Channels%20and%20Some%20Physiographic%20Implications.pdf.]

Maniatis, G., D. Kurfess, A. Hampel, and O. Heidbach (2009), Slip acceleration on normal faults due to erosion and sedimentation: Results from a new three-dimensional numerical model coupling tectonics and landscape evolution, *Earth Planet. Sci. Lett.*, *284*, 570–582.

Masek, J. G., B. L. Isacks, T. L. Gubbels, and E. J. Fielding (1994), Erosion and tectonics at the margins of continental plateaus, *J. Geophys. Res.*, *99*(B7), 13,941–13,956.

Montgomery, D. R., and M. T. Brandon (2002), Topographic controls on erosion rates in tectonically active mountain ranges, *Earth Planet. Sci. Lett.*, *201*, 481–489.

Montgomery, D. R., G. Balco, and S. D. Willett (2001), Climate, tectonics, and the morphology of the Andes, *Geology*, *29*, 579–582.

Molnar, P. (2001), Climate change, flooding in arid environments, and erosion rates, *Geology*, *29*, 1071–1074.

Molnar, P., and P. England (1990), Late Cenozoic uplift of mountain ranges and global climate change: Chicken or egg, *Nature*, *346*, 29–34.

Persson, K. S., D. Garcia-Castellanos, and D. Sokoutis (2004), River transport effects on compressional belts: First results from an integrated analogue-numerical model, *J. Geophys. Res.*, *109*, B01409, doi:10.1029/2002JB002274.

Pysklywec, R. N. (2006), Surface erosion control on the evolution of the deep lithosphere, *Geology*, *34*, 225–228, doi:10.1130/G21963.1.

Ranalli, G. (1995), *Rheology of the Earth*, 2nd ed., Chapman and Hall, Springer.

Roe, G. H., and M. T. Brandon (2011), Critical form and feedbacks in mountainbelt dynamics: Role of rheology as a tectonic governor, *J. Geophys. Res.*, *116*, B02101, doi:10.1029/2009JB006571.

Roe, G. H., K. X. Whipple, and J. K. Fletcher (2008), Feedbacks among climate, erosion, and tectonics in a critical wedge orogen, *Am. J. Sci.*, *308*, 815–842, doi:10.2475/07.2008.01.

Selzer, C., S. J. H. Buiter, and O. A. Pfiffner (2008), Numerical modeling of frontal and basal accretion at collisional margins, *Tectonics*, *27*, TC3001, doi:10.1029/2007TC002169.

Simpson, G. (2004), A dynamic model to investigate coupling between erosion, deposition, and three-dimensional (thin-plate) deformation, *J. Geophys. Res.*, *109*, F02006, doi:10.1029/2003JF000078.

Simpson, G. D. H. (2006), Modelling interactions between fold-thrust belt deformation, foreland flexure and surface mass transport, *Basin Res.*, *18*, 125–143, doi:10.1111/j.1365-2117.2006.00287.x.

Sklar, L. S., and W. E. Dietrich (2004), A mechanistic model for river incision into bedrock by saltating bed load, *Water Resour. Res.*, *40*, W06301, doi:10.1029/2003WR002496.

Steer, Ph., M. Simoes, R. Cattin, and J. B. H. SHyu (2014), Erosion influences the seismicity of active thrust faults, *Nat. Commun.*, *5*, 55–64, doi:10.1038/ncomms6564.

Stolar, D., S. D. Willett, and G. H. Roe (2006), Evolution of a critical orogen under various forcing scenarios: Findings from a numerical sand-box. in *Tectonics, Climate, and Landscape Evolution, Geol. Soc. Am. Spec. Pap., 398*, edited by S. D. Willett et al., pp. 240–250, Geol. Soc. of Am., Boulder, Colo.

Stolar, D., G. Roe, and S. Willett (2007), Controls on the patterns of topography and erosion rate in a critical orogen, *J. Geophys. Res.*, *112*, F04002, doi:10.1029/2006JF000713.

Stüwe, K., J. Robl, S. Hergarten, and L. Evans (2008), Modeling the influence of horizontal advection, deformation, and late uplift on the drainage development in the India-Asia collision zone, *Tectonics*, *27*, TC6011, doi:10.1029/2007TC002186.

Thieulot, C. (2011), Two- and three-dimensional numerical modelling of creeping flow for the solution of geological problems, *Phys. Earth Planet. Inter.*, *188*, 47–68, doi:10.1016/j.pepi.2011.06.011.

Thieulot, C., P. Fullsack, and J. Braun (2008), Adaptive octree-based finite element analysis of two- and three-dimensional indentation problems, *J. Geophys. Res.*, *113*, B12207, doi:10.1029/2008JB005591.

Tomkin, J. H., and J. Braun (1999), Simple models of drainage reorganisation on a tectonically active ridge system, *N. Z. J. Geol. Geophys.*, *42*, 1–10.

Toussaint, G., E. Burov, and J. P. Avouac (2004), Tectonic evolution of a continental collision zone: A thermomechanical numerical model, *Tectonics*, *23*, TC6003, doi:10.1029/2003TC001604.

Tucker, G. E., and R. L. Bras (2000), A stochastic approach to modeling the role of rainfall variability in drainage basin evolution. *Water Resour. Res.*, *36*(7) 1953–1964.

Tucker, G. E., and G. R. Hancock (2010), Modelling landscape evolution, *Earth Surf. Processes Landforms*, *35*, 28–50.

Tucker, G. E. and K. X. Whipple (2002), Topographic outcomes predicted by stream erosion models: Sensitivity analysis and intermodel comparison, *J. Geophys. Res.*, *107*(B9), 2179, doi:10.1029/2001JB000162.

Tullis, J. (2002), Deformation of granitic rocks: Experimental studies and natural examples, in Plastic Deformation of Minerals and Rocks, S.-I. Karato and H.-R. Wenk, *Rev. Mineral. Geochem.*, *51*, 51–95.

Turowski, J. M., D. Lague, and N. Hovius (2007), Cover effect in bedrock abrasion: A new derivation and its implications for the modeling of bedrock channel morphology, *J. Geophys. Res.*, *112*, F04006, doi:10.1029/2006JF000697.

Upton, P., and P. O. Koons (2007), Three-dimensional geodynamic framework for the central southern Alps, New Zealand: Integrating geology, geophysics and mechanical observations, in D. Okaya, T. Stern, and F. Davey, *A Continental Plate Boundary: Tectonics at South Island, New Zealand*, AGU, Washington, D. C.

Upton, P., P. O. Koons, D. Craw, C. M. Henderson, and R. Enlow (2009), Along-strike differences in the Southern Alps of New Zealand: Consequences of inherited variation in rheology, *Tectonics*, *28*, TC2007, doi:10.1029/2008TC002353.

van der Beek, P., and J. Braun (1998), Numerical modelling of landscape evolution on geological time-scales: A parameter analysis and comparison with the south-eastern highlands of Australia, *Basin Res.*, *10*, 49–68, doi:10.1046/j.1365-2117.1998.00056.x.

Vernant, P., F. Hivert, J. Chéry, P. Steer, R. Cattin, and A. Rigo (2013), Erosion-induced isostatic rebound triggers extension in low convergent mountain ranges, *Geology*, *41*(4), 467–470, doi:10.1130/G33942.1.

Whipple, K. X., (2004), Bedrock rivers and the geomorphology of active orogens, *Annu. Rev. Earth Planet. Sci.*, *32*, 151–185, doi:10.1146/annurev.earth.32.101802.120356.

Whipple, K. X., (2009), The influence of climate on the tectonic evolution of mountain belts, *Nat. Geosci.*, *2*, 97–104, doi:10.1038/nge0413.

Whipple, K. X., and B. J. Meade (2004), Controls on the strength of coupling among climate, erosion, and deformation in two-sided, frictional orogenic wedges at steady state, *J. Geophys. Res.*, *109*, F01011, doi:10.1029/2003JF000019.

Whipple, K. X., and B. J. Meade (2006), Orogen response to changes in climatic and tectonic forcing, *Earth Planet. Sci. Lett.*, *243*, 218–228, doi:10.1016/j.epsl.2005.12.022.

Whipple, K. X., and G. E. Tucker (1999), Dynamics of the stream power river incision model: Implications for height limits of mountain ranges, landscape response timescales and research needs, *J. Geophys. Res.*, *104*(B8), 17,661–17,674.

Willett, S. D. (1999), Orogeny and orography: The effects of erosion on the structure of mountain belts, *J. Geophys. Res.*, *104*(B12), 28,957–28,981.

Willett, S. D. (2010), Erosion on a line, *Tectonophysics*, *484*, 168–180.

Willett, S. D., and M. T. Brandon (2002), On steady states in mountain belts, *Geology*, *30*, 175–178.

Willett, S. D., C. Beaumont, and P. Fullsack (1993), Mechanical model for the tectonics of doubly-vergent compressional orogens, *Geology*, *21*, 371–374.

Willgoose, G. (2005), Mathematical modeling of whole landscape evolution, *Annu. Rev. Earth Planet. Sci.*, *33*, 443–459, doi:10.1146/annurev.earth.33.092203.122610.

Zeitler, P. K., et al. (2001), Erosion, Himalayan geodynamics and the geomorphology of metamorphism, *GSA Today 11*, 4–9.